

RNI: DELENG/2005/15153
Publication: 23rd of every month
Posting: 27th/28th of every month at DPSO

No: DL(E)-01/5079/2023-25
Licensed to post without pre-payment U(E) 28/2023-25
Rs.150

ISSN 0973-2136

www.mycoordinates.org

Coordinates

Volume XXI, Issue 12, December 2025

THE MONTHLY MAGAZINE ON POSITIONING, NAVIGATION AND BEYOND



Exploring UAS-Lidar as a sampling tool for satellite-based AGB estimations

Pushing the planning boundaries: A Case of forensic surveying

In Coordinates

10 years before...



mycoordinates.org/vol-XI-issue-12-December-2015

Non-invasive modelling of a monumental masonry aqueduct

Elaiopoulos Michail, Division
"Research and Environment",
CSI Management S.r.l., V.le
C. Pavese 305 – Rome (Italy)

Gentili Mario, Division
"Research and Environment",
CSI Management S.r.l., V.le C.
Pavese 305 – Rome (Italy)

Scibetta Roberto, Division
"Research and Environment",
CSI Management S.r.l., V.le C.
Pavese 305 – Rome (Italy)

Fabrizi Marco, Division
"Research and Environment",
CSI Management S.r.l., V.le
C. Pavese 305 – Rome (Italy)

Pochettino Anna Stellina, Division
"Research and Environment",
CSI Management S.r.l., V.le C.
Pavese 305 – Rome (Italy)

Zecca Giuseppe, Division
"Research and Environment",
CSI Management S.r.l., V.le C.
Pavese 305 – Rome (Italy)

Ancona Leonardo, Office for the management
of the Royal park and the Vanvitelli's Aqueduct,
Museum complex of Caserta, Italian Ministry of
Cultural Heritage and Activities and Tourism

Dr Agnieszka Smigiel, Department of Art
History and cultural heritage, University of
Cagliari, Via Università, Cagliari – Italia

This paper illustrates the combination of non-invasive surveying methodologies for the modeling of an old masonry aqueduct bridge, the "Ponti della Valle", as a support to its structural analysis. The photogrammetric technique of Structure for Motion is used to process photograms taken from specified positions; the created dense point cloud is then edited in order to meet the geometry visualization's needs prescribed by the engineering team of the monument.

Nepal climate data portal in the context of Spatial Data Infrastructure

Rishiraj Dutta, Susantha Jayasinha and Senaka Basnayake Department of Climate Change & Climate Risk Management, Asian Disaster Preparedness Center, Bangkok, Thailand

The Nepal Climate Data Portal may be one such system which can be called as the Climate Base Spatial Data Infrastructure (CSDI). The portal developed for Nepal already addresses the functionality to effectively manage climate data through data ingestion, extraction and metadata management which is also within the required WMO standards of 2014. Considering the portal as a CSDI will open up data sharing needs of the agencies based on cooperative relationships.

Deformation analysis of the Territory of Bulgaria from GNSS observations

Professor Keranka Vassileva, PhD National Institute of Geophysics, Geodesy and Geography, Bulgarian Academy of Science, Sofia, Bulgaria

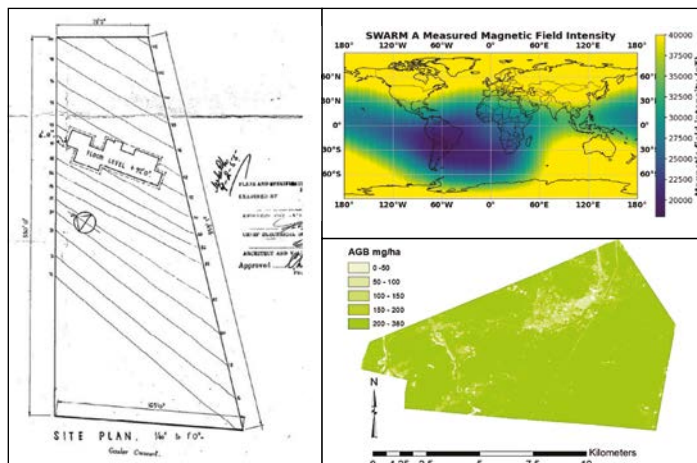
Professor Georgi Valev, D.Sc. Konstantin Preslavsky University of Shumen, Shumen, Bulgaria

The present study is an attempt to contribute to the geokinematics of the territory of Bulgaria by means of Finite Elements Method (FEM) on the base of estimated GNSS station coordinates in different observational epochs.

Zone based indoor location using GNSS simulators

Lisa Perdue, Hironori Sasaki and John Fischer, Spectracom Corp., USA

The flexibility and reliability of the Intelligent Repeater System make it a practical solution that can be deployed as part of building or underground infrastructure either during initial construction or as an addition to the area.



In this issue

Coordinates Volume 21, Issue 12, December 2025

Articles

GNSS Constellation Specific Monthly Analysis Summary: November 2025 NARAYAN DHITAL 5 **Pushing the planning boundaries: A Case of forensic surveying** MIKE STAPLETON 9 **Exploring UAS-lidar as a sampling tool for satellite-based AGB estimations in the Miombo woodland of Zambia** HASTINGS SHAMAOMA, PAXIE W. CHIRWA, JULES C. ZEKENG, ABLE RAMOELO, ANDREW T. HUDAK, FERDINAND HANDAVU AND STEPHEN SYAMPUNGANI 17

Columns

Old Coordinates 2 **My Coordinates** EDITORIAL 4 **News** AI & ROBOTICS 16 GNSS 28 GIS 30 UAV & IMAGING 31 **Industry** 33 **Mark Your Calendar** 34

This issue has been made possible by the support and good wishes of the following individuals and companies

Able Ramoelo, Andrew T. Hudak, Ferdinand Handavu, Hastings Shamaoma, Jules C. Zekeng, Mike Stapleton, Narayan Dhital, Paxie W. Chirwa, and Stephen Syampungani; SBG System, and many others.

Mailing Address

A 002, Mansara Apartments
C 9, Vasundhara Enclave
Delhi 110 096, India.
Phones +91 11 42153861, 98102 33422, 98107 24567

Email

[information] talktous@mycoordinates.org
[editorial] bal@mycoordinates.org
[advertising] sam@mycoordinates.org
[subscriptions] iwant@mycoordinates.org

Web www.mycoordinates.org

Coordinates is an initiative of CMPL that aims to broaden the scope of positioning, navigation and related technologies. CMPL does not necessarily subscribe to the views expressed by the authors in this magazine and may not be held liable for any losses caused directly or indirectly due to the information provided herein. © CMPL, 2025. Reprinting with permission is encouraged; contact the editor for details.

Annual subscription (12 issues)
[India] Rs.1,800* [Overseas] US\$100*

*Excluding postage and handling charges

Printed and published by Sanjay Malaviya on behalf of Coordinates Media Pvt Ltd

Published at A 002 Mansara Apartments, Vasundhara Enclave, Delhi 110096, India.

Printed at Thomson Press (India) Ltd, Mathura Road, Faridabad, India

Editor Bal Krishna

Owner Coordinates Media Pvt Ltd (CMPL)

This issue of Coordinates is of 36 pages, including cover.



Signals under Siege

IATA warns that GPS spoofing and jamming are rising sharply worldwide,

With navigation losses per 1,000 flights nearly doubling in three years,

And India now firmly affected.

What began near conflict zones has spilled into civilian airspace.

Pilots are urged to stay vigilant, aircraft to adapt,

But vigilance cannot replace assured navigation.

Civil aviation rests on signal integrity,

Yet spoofed and denied GNSS is becoming routine.

Passengers may not notice, but safety margins are compromised.

Navigation is critical infrastructure, not a convenience.

And safety is paramount!

Coordinates wishes a year of safety, peace and prosperity for all in 2026.

Bal Krishna, Editor
bal@mycoordinates.org

ADVISORS Naser El-Sheimy PEng, CRC Professor, Department of Geomatics Engineering, The University of Calgary Canada, George Cho Professor in GIS and the Law, University of Canberra, Australia, Professor Abbas Rajabifard Director, Centre for SDI and Land Administration, University of Melbourne, Australia, Luiz Paulo Souto Fortes PhD Associate Professor, University of State of Rio Janeiro (UERJ), Brazil, John Hannah Professor, School of Surveying, University of Otago, New Zealand

GNSS Constellation Specific Monthly Analysis Summary: November 2025

The analysis performed in this report is solely his work and own opinion. State Program: U.S.A (G); EU (E); China (C) "Only MEO- SECM satellites"; Russia (R); Japan (J); India (I)



Narayan Dhital
Actively involved to support international collaboration in GNSS-related activities. He has regularly supported and contributed to different workshops of the International Committee on GNSS (ICG), and the United Nations Office for Outer Space Affairs (UNOOSA). As a professional employee, the author is working as GNSS expert at the Galileo Control Center, DLR GfR mbH, Germany.

Introduction

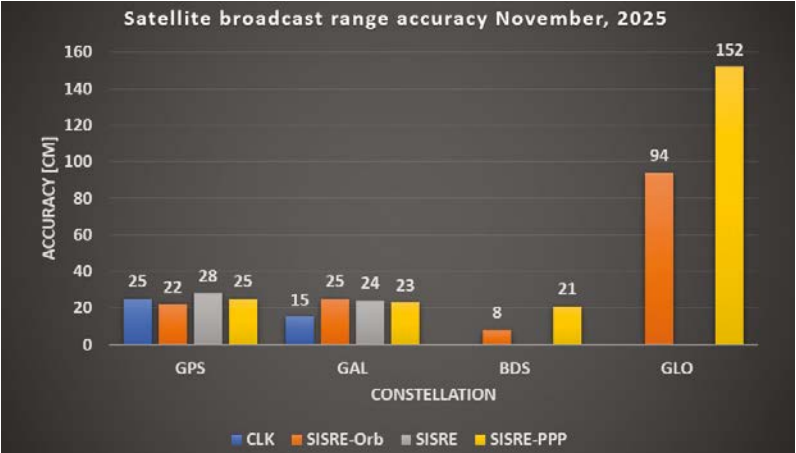
This article continues the monthly performance analysis of the GNSS constellation. Readers are encouraged to refer to previous issues for foundational discussions and earlier results. In addition, there is a short overview on the importance of the Earth’s magnetic field for satellite technologies. This is a continuation of the section F from October issue, 2024.

Analyzed Parameters for November 2025

(Dhital et. al, 2024) provides a brief overview of the necessity and applicability of monitoring the satellite clock and orbit parameters.

- a. Satellite Broadcast Accuracy, measured in terms of **Signal-In-Space Range Error (SISRE)** (Montenbruck et. al, 2010).

(a), (b) Satellite Clock and Orbit Accuracy (monthly RMS values)



- b. **SISRE-Orbit** (only orbit impact on the range error), SISRE (both orbit and clock impact), and **SISRE-PPP** (as seen by the users of carrier phase signals, where the ambiguities absorb the unmodelled biases related to satellite clock and orbit estimations. Satellite specific clock bias is removed) (Hauschlid et.al, 2020)
- c. **Clock Discontinuity**: The jump in the satellite clock offset between two consecutive batches of data uploads from the ground mission segment. It is indicative of the quality of the satellite atomic clock and associated clock model.
- d. **URA**: User Range Accuracy as an indicator of the confidence on the accuracy of satellite ephemeris. It is mostly used in the integrity computation of RAIM.
- e. **GNSS-UTC offset**: It shows stability of the timekeeping of each constellation w.r.t the UTC
- f. **Earth’s Magnetic Field and Radiation Effect**: The field acts as a vital shield, deflecting charged particles from the solar wind and cosmic radiation that would otherwise bombard the atmosphere and surface.

Note:- for India’s IRNSS there are no precise satellite clocks and orbits as they broadcast only 1 frequency which does not allow the dual frequency combination required in precise clock and orbit estimation; as such, only URA and Clock Discontinuity is analyzed.

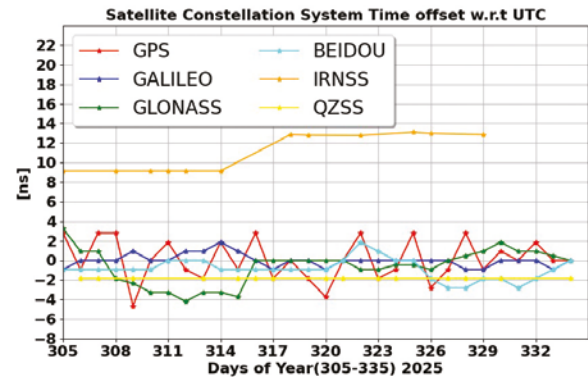
(c) Satellite Clock Jump per Mission Segment Upload

Const	Mean [ns]	Max [ns]	95_ Percentile [ns]	99_ Percentile [ns]	Remark (Best and Worst 95 %)
IRNSS	2.77	841.92	4.54	22.31	Best I06 (1.49 ns) Worst I10 (31.8 ns) Big jumps for each satellite in multiple days.
GPS	0.37	12.03	0.72	2.09	Best G15 (0.41 ns) Worst G03 (3.03 ns). The maximum jump (upto 12 ns) was seen for G13 and G27.
GAL	65.93	4910076.99	0.18	0.40	Best E29 (0.14 ns) Worst E19 (0.34 ns). Large discontinuity for E03, E04, E05 and E27. All of them are informed as not available for the respective days in the NAGU.

(d) User Range Accuracy (Number of Occurrences in Broadcast Data 01–30 November)

IRNSS-SAT	2 [m]	2.8 [m]	4.0 [m]	5.7 [m]	8 [m]	8192 [m]	9999.9 [m]	Remark Other URA values (frequency)
I02	2901	15	3	-	1	-	2	-
I06	2878	31	-	-	2	-	2	-
I09	846	10	3	-	-	-	-	-
I10	651	4	-	-	1	-	-	-

(e) GNSS-UTC Offset



(F) Earth’s Magnetic Field and Radiation Effect

The Earth’s magnetic field originates deep within the planet, where molten iron in the outer core moves in vast, turbulent currents. These motions generate electric currents that power the geodynamo, producing a magnetic field that extends far into space. More than just a scientific curiosity, this field acts as a vital shield, deflecting charged particles from the solar

wind and cosmic radiation that would otherwise bombard the atmosphere and surface. Although often simplified as a dipole aligned with Earth’s rotation axis, the field is far more complex: its strength and orientation vary across different regions, and it evolves continuously over time. This dynamic nature makes the magnetic field both a subject of geophysical study and a critical factor in protecting satellites and modern technology. The importance of this shielding is underscored by recent aviation incidents, such as the Airbus flight where a cosmic ray caused a bit flip in onboard electronics, reminding us that radiation can disrupt systems even at aircraft cruising altitudes.

To measure the magnetic field with precision, ESA launched the Swarm constellation in 2013. Each Swarm satellite carries both vector magnetometers, which record the direction of the field, and absolute scalar magnetometers, which measure its intensity. Together, these instruments provide highresolution data on the field’s magnitude and orientation, allowing scientists to compare observations with geomagnetic models such as CHAOS and IGRF. This comparison reveals how the field evolves, highlights anomalies, and helps track the longterm weakening of certain regions.

One of the most striking anomalies is the South Atlantic Anomaly (SAA), a region over South America and the South Atlantic where the magnetic field is unusually weak. The anomaly arises because Earth’s magnetic dipole is offset from the planet’s center and because reversed flux patches exist at the core–mantle boundary. As a result, the field intensity at satellite altitudes can drop below 22,000 nanotesla, far weaker than elsewhere. This weakening allows the inner Van Allen radiation belt to dip closer to Earth, exposing satellites to higher radiation flux. A global magnetic field map, as in Figure Fa computed with SWARM A data from ESA database, vividly illustrates this weakened region, showing how the SAA stands out as a hotspot of vulnerability.

The consequences for satellite infrastructure are significant. Electronics such as chips and memory systems are particularly sensitive to radiation. In the SAA, satellites experience Single Event Effects (SEE), including bit flips, latches, and memory loss. ESA’s Swarm mission has recorded frequent singleevent

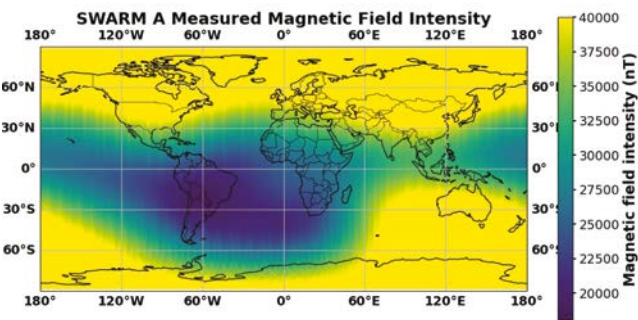


Figure F a: The variability of the Earth’s magnetic field measured by satellite SWARM A for October–November 2025. The SAA region and western Africa show the weakening magnetic field.

upsets in onboard memory during anomaly crossings, confirming the operational risks. GNSS systems are also affected: radiation and plasma irregularities can cause temporary loss of GPS lock, degraded tracking, and increased noise. Swarm's GPS receivers have documented such disruptions, though they are typically shortlived and corrected in postprocessing.

Oscillators and frequency generators, which provide the timing backbone for satellite payloads, are another critical vulnerability. UltraStable Oscillators (USOs) are designed to deliver precise frequency references, but radiation in the SAA perturbs their stability. This leads to frequency drift and degraded orbit determination. Sentinel3A and Sentinel6A missions, operating at higher altitudes, have reported USO frequency anomalies correlated with SAA crossings. These findings echo earlier GNSS constellation analysis (Section F, October Issue, 2024), where clock oscillations were shown to impact navigation performance. The SAA provides a physical driver for such oscillations: radiation exposure perturbs oscillator stability, which in turn affects GNSS timing and positioning.

In summary, the Earth's magnetic field is both a scientific phenomenon and a critical infrastructure shield. Its weakening in the South Atlantic Anomaly exposes satellites to radiation that impacts electronics, GNSS receivers, and oscillators. Swarm's measurements provide the scientific foundation for understanding these changes, while Sentinel's oscillator anomalies demonstrate the operational consequences. Together, they highlight the importance of monitoring the magnetic field not only for geophysical insight but also for the resilience of satellite technology.

Further readings:

<https://www.sciencedirect.com/science/article/abs/pii/S0273117718302941>

https://www.esa.int/Enabling_Support/Space_Engineering_Technology/Swarm_vs._space_radiation_the_first_10_years?

<https://mycoordinates.org/gnss-constellation-specific-monthly-analysis-summary-october-2024/>

Monthly Performance Remarks:

1. Satellite Clock and Orbit Accuracy:
 - The performance of GPS, Galileo and Beidou remained similar.
 - Not much jumps in GPS satellite clocks. Galileo satellites had couple of discontinuities that were covered by NAGUs (unavailability of the satellites)
2. The UTC Prediction (GNSS-UTC):
 - IRNS provided comparatively worse performances. Other constellations show consistent and stable predictions.

References

Alonso M, Sanz J, Juan J, Garcia, A, Casado G (2020) Galileo Broadcast Ephemeris and Clock Errors Analysis: 1 January 2017 to 31 July 2020, MDPI

Alonso M (2022) Galileo Broadcast Ephemeris and Clock Errors, and Observed Fault Probabilities for ARAIM, Ph.D Thesis, UPC

Bento, M (2013) Development and Validation of an IMU/GPS/Galileo Integration Navigation System for UAV, PhD Thesis, UniBW.

BIMP (2024 a) https://e-learning.bipm.org/pluginfile.php/6722/mod_label/intro/User_manual_cggtts_analyser.pdf?time=1709905608656

BIMP (2024 b) <https://e-learning.bipm.org/mod/folder/view.php?id=1156&forceview=1>

BIMP (2024 c) <https://cggtts-analyser.streamlit.app>

Bruggemann, Troy & Greer, Duncan & Walker, R.. (2011). GPS fault detection with IMU and aircraft dynamics. IEEE Transactions on Aerospace and Electronic Systems - IEEE TRANS AEROSP ELECTRON SY. 47. 305-316. 10.1109/TAES.2011.5705677.

Cao X, Zhang S, Kuang K, Liu T (2018) The impact of eclipsing GNSS satellites on the precise point positioning, Remote Sensing 10(1):94

Chen, K., Chang, G. & Chen, C (2021) GINav: a MATLAB-based software for the data processing and analysis of a GNSS/IMU integrated navigation system. *GPS Solut* 25, 108. <https://doi.org/10.1007/s10291-021-01144-9>

Curran, James T. & Broumendan, Ali. (2017). On the use of Low-Cost IMUs for GNSS Spoofing Detection in Vehicular Applications.

Dhital N (2024) GNSS constellation specific monthly analysis summary, Coordinates, Vol XX, Issue 1, 2, 3, 4

Dhital N (2025) GNSS constellation specific monthly analysis summary, Coordinates, Vol XXI, Issue 1

GINAv (2025). <https://geodesy.noaa.gov/gps-toolbox/GINav.shtml>

Goercke, L (2017) GNSS-denied navigation of fixed-wing aircraft using low-cost sensors and aerodynamic motion models, PhD Thesis, TUM.

GROOPS (2025) GROOPS Documentation and Cookbook. <https://groops-devs.github.io/groops/html/index.html>

GSC (2023) Galileo Q3 Performance Report. https://www.gsc-europa.eu/sites/default/files/sites/all/files/Galileo-OS-Quarterly-Performance_Report-Q3-2023.pdf

Guo, Jing & Chen, Guo & Zhao, Qile & Liu, Jingnan & Liu, Xianglin. (2017). Comparison of solar radiation pressure models for BDS IGSO and MEO satellites with emphasis on improving orbit quality. GPS Solutions. 21. 10.1007/s10291-016-0540-2.

Guo F, Zhang X, Wang J (2015) Timing group delay and differential code bias corrections for BeiDou positioning, J Geod,

Hauschlid A, Montenbruck O (2020) Precise real-time navigation of LEO satellites using GNSS broadcast ephemerides, ION

IERS C04 (2024) <https://hpiers.obspm.fr/iers/eop/eopc04/eopc04.1962-now>

IGS (2019) GNSS Attitude Quaternions Exchange using ORBEX

IGS (2021) RINEX Version 4.00 https://files.igs.org/pub/data/format/rinex_4.00.pdf

InsideGNSS (2024) Working papers: upgrading galileo <https://insidegnss.com/working-papers-upgrading-galileo/>

Jiabo G, Xingyu Z, Yan C, Mingyuan Z (2021) Precision Analysis on Reduced-Dynamic Orbit Determination of GRACE-FO Satellite with Ambiguity Resolution, *Journal of Geodesy and Geodynamics* (<http://www.jgg09.com/EN/Y2021/V41/I11/1127>)

Kj, Nirmal & Sreejith, A. & Mathew, Joice & Sarpotdar, Mayuresh & Suresh, Ambily & Prakash, Ajin & Safonova, Margarita & Murthy, Jayant. (2016). Noise modeling and analysis of an IMU-based attitude sensor: improvement of performance by filtering and sensor fusion. 99126W. 10.1117/12.2234255.

Li M, Wang Y, Li W (2023) performance evaluation of real-time orbit determination for LUTAN-01B satellite using broadcast earth orientation parameters and multi-GNSS combination, *GPS Solutions*, Vol 28, article number 52

Li W, Chen G (2023) Evaluation of GPS and BDS-3 broadcast earth rotation parameters: a contribution to the ephemeris rotation error Montenbruck

Liu, Yue & Liu, Fei & Gao, Yang & Zhao, Lin. (2018). Implementation and Analysis of Tightly Coupled Global Navigation Satellite System Precise Point Positioning/Inertial Navigation System (GNSS PPP/IMU) with IMU sufficient Satellites for Land Vehicle Navigation. *Sensors*. 18. 4305. 10.3390/s18124305.

Mayer-Guerr, T., Behzadpour, S., Eicker, A., Ellmer, M., Koch, B., Krauss, S., Pock, C., Rieser, D., Strasser, S., Suesser-Rechberger, B., Zehentner, N., Kvas, A. (2021). GROOPS: A software toolkit for gravity field recovery and GNSS processing. *Computers & Geosciences*, 104864. <https://doi.org/10.1016/j.cageo.2021.104864>

Montenbruck O, Steigenberger P, Hauschlid A (2014) Broadcast versus precise ephemerides: a multi-GNSS perspective, *GPS Solutions*

Liu T, Chen H, Jiang Weiping (2022) Assessing the exchanging satellite attitude quaternions from CNES/CLS and their application in the deep eclipse season, *GPS Solutions* 26(1)

Montenbruck O, Steigenberger P (2024) The 2024 GPS accuracy improvement initiatives, *GPS Solutions*

Montenbruck O, Steigenberger P, Hauschlid A (2014) Broadcast versus precise ephemerides: a multi-GNSS perspective, *GPS Solutions*

Montenbruck O, Hauschlid A (2014 a) Differential Code Bias Estimation using Multi-GNSS Observations and Global Ionosphere Maps, *ION*

Montenbruck, O., Schmid, R., Mercier, F., Steigenberger, P., Noll, C., Fatkulin, R., Kogure, S. & Ganeshan, A.S. (2015) GNSS satellite geometry and attitude models. *Advances in Space Research* 56(6), 1015-1029. DOI: 10.1016/j.asr.2015.06.019

Niu, Z.; Li, G.; Guo, F.; Shuai, Q.; Zhu, B (2022) An Algorithm to Assist the Robust Filter for Tightly Coupled RTK/IMU Navigation System. *Remote Sens.* **2022**, *14*, 2449. <https://doi.org/10.3390/rs14102449>

Schmidt, G, Phillips, R (2010) IMU/GPS Integration Architecture Performance Comparisons. *NATO*.

Space (2025) <https://www.space.com/astronomy/earth/mysterious-boost-to-earths-spin-will-make-aug-5-one-of-the-shortest-days-on-record>

Steigenberger P, Montenbruck O, Bradke M, Ramatschi M (2022) Evaluation of earth rotation parameters from modernized GNSS navigation messages, *GPS Solutions* 26(2)

Strasser S (2022) Reprocessing Multiple GNSS Constellations and a Global Station Network from 1994 to 2020 with the Raw Observation Approach, PhD Thesis, Graz University of Technology

Suvorkin, V., Garcia-Fernandez, M., González-Casado, G., Li, M., & Rovira-Garcia, A. (2024). Assessment of Noise of MEMS IMU Sensors of Different Grades for GNSS/IMU Navigation. *Sensors*, 24(6), 1953. <https://doi.org/10.3390/s24061953>

Sylvain L, Banville S, Geng J, Strasser S (2021) Exchanging satellite attitude quaternions for improved GNSS data processing consistency, Vol 68, Issue 6, pages 2441-2452

Tanil, Cagatay & Khanafseh, Samer & Pervan, Boris. (2016). An IMU Monitor against IMU GNSS Spoofing Attacks during GBAS and SBAS-assisted Aircraft Landing Approaches. 10.33012/2016.14779.

Walter T, Blanch J, Gunning K (2019) Standards for ARAIM ISM Data Analysis, *ION*

Wang, C & Jan, S (2025). Performance Analysis of MADOCA-Enhanced Tightly Coupled PPP/IMU. *NAVIGATION: Journal of the IMUtitute of Navigation* March 2025, 72 (1) navi.678; DOI: <https://doi.org/10.33012/navi.678>

Wang N, Li Z, Montenbruck O, Tang C (2019) Quality assessment of GPS, Galileo and BeiDou-2/3 satellite broadcast group delays, *Advances in Space Research*

Wang J, Huang S, Lia C (2014) Time and Frequency Transfer System Using GNSS Receiver, *Asia-Pacific Radio Science*, Vol 49, Issue 12

<https://cggtts-analyser.streamlit.app>

Yang N, Xu A, Xu Z, Xu Y, Tang L, Li J, Zhu H (2025) Effect of WHU/GFZ/CODE satellite attitude quaternion products on the GNSS kinematic PPP during the eclipse season, *Advances in Space Research*, Volume 75, Issue 1,

Yao J, Lombardi M, Novick A, Patla B, Sherman J, Zhang V (2016) The effects of the January 2016 UTC offset anomaly on GPS-controlled clocks monitored at NIST. <https://tf.nist.gov/general/pdf/2886.pdf>

Note: References in this list might also include references provided to previous issues.


Data sources and Tools:

<https://cddis.nasa.gov> (Daily BRDC); http://ftp.aiub.unibe.ch/CODE_MGEX/CODE/ (Precise Products); BKG “SSRC00BKG” stream; IERS C04 ERP files

(The monitoring is based on following signals- GPS: LNAV, GAL: FNAV, BDS: CNAV-1, QZSS:LNAV IRNSS:LNAV GLO:LNAV (FDMA))

Time Transfer Through GNSS Pseudorange Measurements: <https://e-learning.bipm.org/login/index.php>

Allan Tools, <https://pypi.org/project/AllanTools/>

gLAB GNSS, <https://gage.upc.edu/en/learning-materials/software-tools/glab-tool-suite> 

Pushing the planning boundaries: A case of forensic surveying

This paper outlines the case of a Canberra homeowner and their architect stretching the planning rules beyond the limits and a surveyor's critical role in a court case relating to the rules for home construction.



Mike Stapleton

Lovell Property Consultants, Surveyor and Town Planner in the ACT and was previously registered as a Land Surveyor in South Africa. Mike has over 45 years experience in surveying. He has served as CPD co-ordinator for Institute of Surveyors, Canberra, and chair of the ACT region and Area of Practice of Surveying on Surveying and Spatial Sciences Institute and the Geospatial Council of Australia. He has now "semi-retired", but still undertakes consultancy work relating to cadastral and planning projects in both ACT and New South Wales.

Abstract

Legislation plays a vital role in cadastral surveying and town planning, and on occasion surveyors are asked to give evidence at court. This paper outlines the case of a Canberra homeowner and their architect stretching the planning rules beyond the limits and a surveyor's critical role in a court case relating to the rules for home construction. In Deakin, an old and prestigious suburb of Canberra, 2-storey dwellings are the maximum size permitted. However, what constitutes a 'storey' and 'basement' are critical to the extent one can build. In this case, a dwelling was erected. The owner, their architect, a certifier and the Government Planning Authority believed that the dwelling satisfied the planning rules. A neighbour disagreed and took the matter to the ACT Civil & Administrative Tribunal. Critical to the case was the determination of the 'datum ground level' and the position of the contour a metre below the floor level above the lowest level. This paper describes the investigation to determine the datum ground level, involving research of contour plans dating back as far as 1910 and aerial imagery dating back to 1951. The datum ground level determination required ascertaining the levels at the time of operational acceptance for subdivision, which in this case was 1951. The methodology used to determine the datum ground level and its location involved the following 9-step process: (1) Analyse the definition, (2) determine the time stamp required for datum ground level, (3) plan the research, (4) locate the site on the contour plan, (5) determine a consistent datum, (6) search and analyse aerial imagery, (7)

trace locations into a Computer-Aided Design (CAD) file, (8) interpolate the data, and (9) decide on the best solution for the datum ground level and its location. It was concluded that the critical datum ground level contour passed through the bedroom on the upper level, meaning that the dwelling should be deemed to be a 3-storey building and not permitted on the site.

1 Introduction

Legislation plays a vital role in cadastral surveying and town planning, and on occasion surveyors are asked to give evidence at court. This paper provides an example by outlining the case of a Canberra homeowner and their architect stretching the planning rules beyond the limits and the surveyor's critical role in a court case relating to the rules for home construction.

A new residence has been constructed on Block 5 Section 9 at 8 Gawler Crescent in Deakin, Australian Capital Territory (ACT) (Figure 1). A dispute has arisen as to whether the building is a 2-storey or 3-storey building. On visual inspection, the building clearly has three levels. However, the owner and the architects who designed the building contend that part of the lower level is a basement and that the third level is constructed over the basement. If the third level is constructed over a basement, the building can be considered as a 2-storey building.

Basement means a space within a building where the floor level of the space is predominantly below datum ground level and where the finished floor level of the level immediately above the space is less

than 1.0 m above datum ground level. Whether part of the lower level is a basement and, if it is, where that part of the basement is located with respect to the upper level is dependent on the position of datum ground level. This paper examines the issue of datum ground level and makes a determination as to its location.

2 Definition of datum ground level

The Territory Plan defines datum ground level as the surface ground level as determined in a field survey authorised by a registered surveyor (ACT Government, 2024a):

- a. at the time of operational acceptance for subdivision, or
- b. if a) is not available, provided no new earthworks have occurred, or
- c. at the date of grant of the lease of the block,

whichever is the earliest.

Where a), b) or c) is not available, datum ground level is the best estimate of the surface ground level determined in a field survey, considering the levels of the immediate surrounding area and authorised by a registered surveyor.

The author believes that a) and c) in this instance will be the same. Option b) does not apply as earthworks have occurred. The options a) or c) can be deduced from old plans or databases before or after the date and confirmed by comparing recent surveys of undisturbed areas in proximity of the site

The following assumptions are made:

- Datum ground level means the existing level of a site at any point. It is not a single level.

- A registered surveyor includes the equivalent status utilised at the time of the survey. (Charles Scrivener was a licensed surveyor.) Government departments with registered/licensed surveyors are included in the definition.
- A field survey includes photogrammetric or Light Detection and Ranging (LiDAR) surveys conducted by aircraft or drones.

It should be noted that the Surveyor-General of the ACT has issued a guideline in 2013 relating to the determination of datum ground level. As it is inconsistent with the Territory Plan (ACT Government, 2024a) and National Capital Plan (Australian Government, 2020), the Territory Plan definition is considered to be that which should be used in the determination. Unfortunately, due to its existence, confusion exists as to the definition to be adopted and thus the value of datum ground level.

The definition in the guideline states (ACT Government, 2013): “Datum ground level means the level of the surface of the ground as defined in a field survey and authorised by a qualified surveyor at the time of operational acceptance for greenfield development or prior to any new earthworks having occurred after that time.”

The key difference between the definitions is that the Territory Plan provides three options and specifically states that if available the earliest should be adopted. The guideline definition requires that for non-Greenfields developments the level is that level prior to any new earthworks having occurred after that time. Thus under the Territory Plan definition, the datum ground level is the level before construction in 1955, while under the guideline the level is that level of the ground before construction commenced for the new dwelling, which is the level defined in the plan produced by Capital Surveys in 2020 (see section 4.7).

A second difference is that the Territory Plan requires the authorisation of a registered surveyor, whilst the guideline requires the authorisation of a ‘qualified surveyor’, whose definition includes surveyors other than registered surveyors.

3 History of the site

Deposited Plan (DP) 316 was signed by the licensed surveyor on 14/05/1951 and certified by the Acting Surveyor-General on 01/08/1951 (Figure 2). It is likely that ‘operational acceptance’ occurred earlier in 1951 or late 1950. The date of survey was 10/10/1950. The lease of Block 5 Section 9 was granted on 14/07/1951.

Over the years, several aerial images were collected over the site (Figure 3). Older aerial imagery revealed the following:

- 1951: Only scattered tracks crossed the site. No significant earthworks had occurred.
- 1952: Works appeared to have commenced with the construction of Westminster House on the adjacent Block 4 south-east of the site.
- 1955: Dwellings had been constructed on adjacent Blocks 4 and 18, while earthworks had commenced on the subject site.
- 1958: The dwellings on Blocks 5 and 6 appeared to have been constructed.
- 1962: Extensions were added to 8 Gawler Crescent (at the rear of the existing building).

Recent history included:

- May 2021: Environment, Planning and Sustainable Development (EPSD) consideration.
- September 2021: Certifier approval for the proposed dwelling.
- May 2023: Certifier approval of amendments.

Recent aerial imagery indicated:

- 2004 & 2015: Original home with access driveway. Apparent undisturbed areas around a regulated tree south of the dwelling on Block 6 and in the rear of Block 18.
- 2022: Original home demolished,

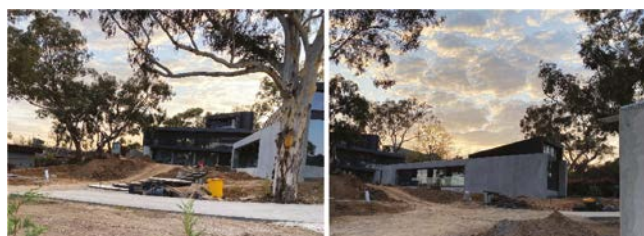


Figure 1: New residence constructed in Deakin

construction of new dwelling underway with extensive earthworks, but undisturbed areas remain under the tree on Block 6 and in the rear of Block 18.

4 Contour plans

The following contour plans indicating levels have been found relating to the site:

- 1910 contour map of Canberra – Charles Scrivener (1910).
- Site plan 10 Gawler Crescent – Unknown (1955-1958).
- Site plan 8 Gawler Crescent – Unknown (1955).

- ACT Contour Series (7C) – Department of the Interior (1960).
- ACT Contour Series (8A2) – Department of the Interior (1960).
- Canberra-by-Suburbs – ACT Survey Office (pre-2000).
- ACTmapi 2015 contours – ACT Survey Office (2015).
- 2015 LiDAR data – ACT Survey Office / Geoscience Australia (2015).
- Contour and detail surveys – Capital Surveys (2020).

The following sections describe these contour plans in more detail.

4.1 Contour Map of Canberra (1910)

The only comprehensive source of heights (levels) found prior to 1951 was the 1910 contour map of Canberra prepared under the supervision of Charles Scrivener (Scrivener, 1912) (Figure 4). As existing trigonometrical (trig) stations were shown on the plan, it is possible to 'locate' the subject site on the plan and hence use the contours from the plan. These contours would be indicative of the levels at the time of issue of the lease and commencement of the subdivision in 1951. The contour intervals are 5 ft, indicating a reasonably high level of accuracy.

The levels are given in feet and thus can be converted to metres. However, the height datum for levels has changed over the years with the ACT adopting

the Australian Height Datum (AHD) in 1971 (Daly, 1972; Evans, 2022). To relate the Scrivener and 1964 levels to the current levels would thus require adaptation. On the other hand, the Canberra-by-Suburbs levels and current surveys relate to the AHD. The adaption may normally involve comparing level values of bench marks from early surveys to what they are and adjusting contours accordingly. For example 'West of School' trig is shown on the Scrivener plan as having a level of 1,978 ft, which converts to 602.894 m, whilst its level now provided in the ACTmapi database (ACT Government, 2024b) is 602.265 m.

A more realistic approach was to adopt areas close by, which do not appear to have been affected by earthworks and compare levels shown on the various level sources to determine an appropriate datum. The ACTmapi contours appear to have been based on the 2015 LiDAR data, so could be used as a source for comparison with the 1910 survey.

In summary, this 1910 plan provides an early indication of the levels of the site. However, the accuracy is questionable due to:

- The distortion in creating the image.
- The scale of the plan relative to the site.
- The methodology for determining heights was less accurate than the methods used today.
- The levels of bench marks have changed over time, and the height datum has been changed to AHD.

Nevertheless, the 1910 contours do give an indication of the even slope over the site.

4.2 Site Plan 10 Gawler Crescent (1955-1958)

This site plan was obtained from an image of the house design provided by Berkely Real Estate on the allhomes website. Unfortunately, the image is not clear and as a result neither the contour values nor the responsible surveyor's name can be read. Values for the contour intervals can be gauged by comparing the contours on recent plans (either Capital



Figure 2: DP316.



Figure 3: Aerial imagery collected over the site in 1951, 1955, 2021 and 2022.

Surveys or ACTmapi contours), thus providing an indication of the levels along the boundary between Blocks 5 and 6.

4.3 Site Plan 8 Gawler Crescent (1955)

This site plan forms part of building plans submitted by Ancher, Mortlock and Murray, Architects. The plan is rough, with boundaries not scaling to match the dimensions of the block (Figure 5). No indication is provided as to the derivation of the contours, or whether the survey was authorised by a registered surveyor. Contours are provided at 2 ft intervals based on a local datum. However, the floor level of the dwelling is provided as 92 ft.

As the later survey by Capital Surveys determined a height of the floor level, it was possible to derive contour values based on the Capital Surveys floor level (average of 618.8 m). Thus, whilst the plan appears to be rough and the accuracy may be queried, the plan does provide the most direct indication of datum floor level.

4.4 ACT Contour Series (7C and 8A2) (1960)

Plan 7C indicates contours and also that a dwelling had been constructed on the site before that time. Hence earthworks would have occurred around the site of the dwelling, which is also the approximate location of the existing dwelling. Plan 7C has 5 ft contour intervals, while Plan 8A2 (which extends into Block 4 south-east of the site) has 1 ft contour intervals. Plan 7C indicates fencing on or close to the boundaries, so a good indication of the relative position of the boundaries and

contours can be plotted. Plan 8A2 shows the boundaries as opposed to boundary fences, thus providing greater accuracy. Plan 8A2 also again illustrates the even gradient of the land near the subject site. As these plans were prepared after the construction of the dwellings and as the conversion to AHD occurred after 1960, these plans have not been used.

4.5 Canberra-by-Suburbs Contour Set (Pre-2000)

A Computer-Aided Design (CAD) file dataset of boundaries, contours, building outlines and other features was provided by the ACT government before the commencement of ACTmapi.

The origin of the contours is unknown, but it is known to have been provided before 2000. The contours were not used as they were determined after construction work was undertaken and have been superseded by the LiDAR survey of 2015.

4.6 ACTmapi Contours and LiDAR Levels (2015)

The ACTmapi contour database is based on 2015 LiDAR survey data and provides a good indication of the levels on the site and surrounding areas before construction began on the newly constructed dwelling (Figures 6 & 7). It also enables the determination of level values of apparently undisturbed land close to the site of the residence (at the rear of Blocks 5 and 14, and around the regulated tree near the boundary adjacent to the residence at 10 Gawler Crescent). The ACTmapi contours are a smoothed version of the contours from the Geoscience Australia point cloud.

4.7 Contour and Detail Plan of Block 5 by Capital Surveys (2020)

This survey covers the area on which the new dwelling has been built (Figure 8). It is referred to AHD and largely consistent with the ACTmapi 2015 contours. The survey was undertaken before the old dwelling was demolished and one can determine contours through apparently undisturbed areas. The plan was certified by a registered surveyor.

Thus it was possible to suggest that the contours at the rear (north-east) of Block 5 (621 m) and the contour running close to the regulated trees (615 m) are largely undisturbed. Assuming the even slope shown in the Scrivener and other plans, a justifiable datum ground level for the site could be interpolated between the 615 m and 621 m contours.

5 Methodology

Following the decision to use the Territory Plan definition, the methodology used to determine the datum ground level and its location involved the following process: (1) Determine the time stamp required for datum ground level, (2) plan the research, (3) locate the site on the contour plan, (4) determine a consistent



Figure 4: Contour map of Canberra (1910).

datum, (5) search and analyse the aerial imagery, (6) trace locations into a CAD file, (7) interpolate the data, and (8) decide on the best solution for the datum ground level and its location.

5.1 Determine the time stamp required for Datum Ground Level

The Crown Lease and Deposited Plan (DP316) were examined to determine the date of operational acceptance for subdivision and the date of grant of the lease of the block. This was determined to be between October 1950 and August 1951.

5.2 Plan the research

A thorough investigation was made of sources of levels, encompassing 90 years between Scrivener’s original

contour survey in 1910 and the survey of the subject site by Capital Surveys in 2020. The acquired contour plans have already been discussed in section 4.

5.3 Locate the site on the contour plan

The locations of the Scrivener contours could be approximately determined using trig stations and survey marks shown on the plan that either still exist today or for which coordinates are still available (Figure 9). Some versions of the Scrivener maps also included grids and street overlays. The ACTmapi historical plans website provides an overlay of the cadastral boundaries over old maps.

5.4 Determine a Consistent Datum

The acquired plans had varying coordinate and level datums. These datums needed to be correlated to ensure consistent comparisons could be made and the site analysed.

5.5 Search and Analyse the Aerial Imagery

It was necessary to determine when construction began and the extent of excavations on the site and neighbouring properties. ACTmapi provides historical aerial imagery dating back to the early 1950s (see Figure 3). From these images, it was possible to determine the extent and year of excavation, along with identifying unexcavated areas. Based on this information, contours shown within the excavated areas on plans prepared after the date of excavation were discounted. Modern imagery is available via ACTmapi as well as other sources such as Nearmap. By comparing the recent imagery with the imagery from the 1950s one could determine areas on or close to the site where little or no excavation had taken place. Levels in those areas could thus be used as an indication of the datum ground level.

5.6 Trace Locations into a CAD File

Based on the information provided on the site plan of the architects, Collins Pennington, and the survey report plan of Kleven Spain, it was not possible to accurately plot the position of the new dwelling. Unfortunately, CAD data was not provided. However, modern CAD packages such as AutoCAD allow the user to import other files (including images) into the CAD file.

The site and floor plans of the dwelling were thus scanned as jpg files and imported into the CAD file. As these drawings showed the location of the dwelling as well as the boundaries, it was possible to scale and rotate the images to reflect the scale and orientation of the CAD file. The ACTmapi database includes accurate cadastral information, allowing the site coordinates to be determined on the required grid. The now scaled and rotated images were then overlaid with the boundaries obtained from the ACTmapi database, and the positions of the dwelling and associated floors were traced into the CAD file.

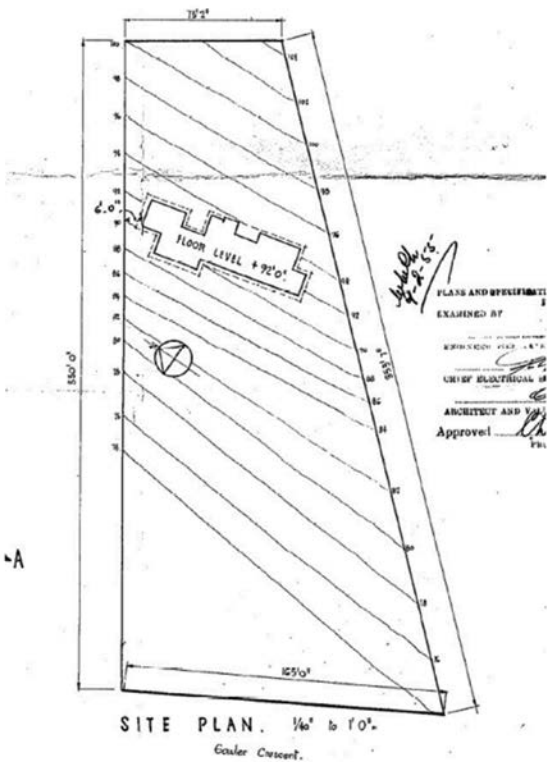


Figure 5: Site Plan 8 Gawler Crescent (1955).



Figure 6: ACTmapi contours (2015) derived from LiDAR data.

In a similar way, contours shown on acquired plans could be traced into the CAD file and used to determine the datum ground level. Thus, datum ground levels for strategic points of the new dwelling could be interpolated from this data.

5.7 Interpolate the Data

Contours are not a precise determination of heights surveyed. The denser the survey of heightened points, the more accurate is the resulting contour. Contours are determined by interpolating on a straight line between points for which a height has been surveyed. This process is repeated multiple times between the

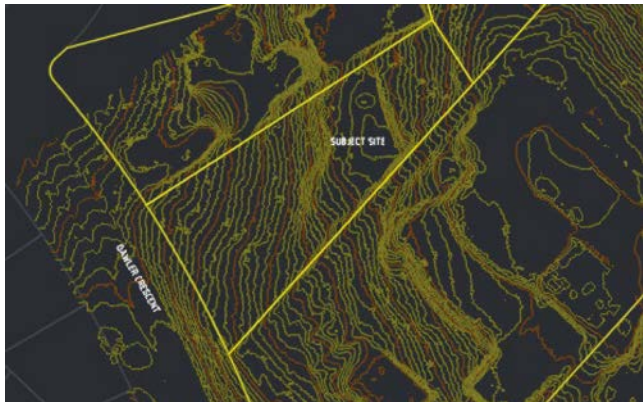


Figure 7: LiDAR contours (2015) from Geosciences Australia



Figure 8: Contour and detail plan of Block 5 by Capital Surveys (2020).

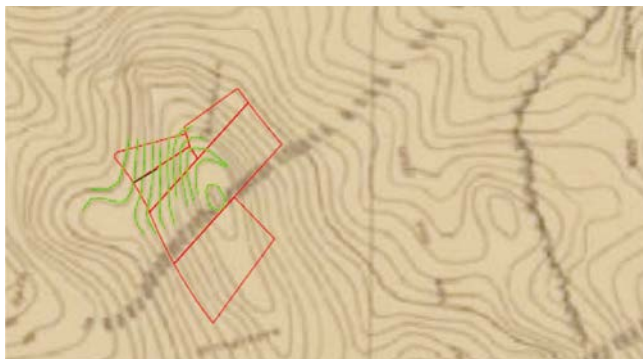


Figure 9: Location of the subject site overlayed on Scrivener's contour plan.

points surveyed to obtain the contour on which datum ground level can be based. Modern software does this process very quickly using a triangular mesh over the points surveyed.

Similarly to determining the contour by interpolation, heights associated with various parts of a building can be determined by interpolating either between surveyed points (if available) or by interpolating between the contours.

- In order to determine the datum ground level, the following two interpolation processes were applied:
- Interpolation between adopted contour lines (in unexcavated areas) to approximate the contours over areas which had been excavated.
 - Interpolation of datum ground levels from the contours adopted or interpolated for positions of the dwelling.

5.8 Decide on the Best Solution for Datum Ground Level

- Based on this interpolation, the following two result options were determined:
4. The contours obtained from the recent surveys (Capital Surveys confirmed by ACTmapi contours), being the 615 m and 621 m contours, were interpolated evenly to obtain the contours between these values. This approach is justified due to the even distribution of contours shown on earlier plans, and it can be shown that the plans used were produced under the authorisation of a registered surveyor. The results are shown in Figure 10.
 5. The contours were determined using the site plan in the building plans of the dwelling constructed in the 1950s and shown relative to the floor level. Capital Surveys surveyed three floor levels in the old dwelling with very consistent results. A rounded average of 618.8 m was adopted, and the contour values of the building plans were then converted to this datum. It is likely that the Capital Surveys plan was the contour survey used by the architects for the design of the new dwelling. Thus using the building site plan to reflect datum ground level before excavation began, the datum ground levels for positions of the new dwelling were determined. This method is more direct and positively reflects levels at the time relative to the building floor level. However, option 1 was also provided as the origin of the levels used in option 2 is uncertain, and it is further unknown if the survey was conducted under the authority of a registered or licensed surveyor. The results are shown in Figure 11.

In the author's opinion, option 2 should be adopted. The two options produced reasonably consistent results for the datum ground level. Importantly, both options determined the critical 619 m contour further to the east from that adopted in the design of the new dwelling. The location of the 619 m contour (from both options) passes through the bedroom located on the upper level of the new dwelling. Consequently, the dwelling should be considered to have three storeys and is therefore in contravention of the building code for the area.

On the provision of the author’s report as evidence for the case, the ‘other side’ produced reports from surveyors expressing their views and rebutting the evidence provided. As a consequence of these reports, further investigation was required into the views expressed therein and the author was asked to address queries raised and provide his own rebuttals. One of the issues which arose was the creation of contours from a triangular mesh and how different critical contours could be portrayed if alternative contours were adopted.

6 The design and the contention enabling the upper floor

The architect made a determination that the lowest contour relevant to enabling part of the lowest floor to be considered as basement was the 619 m contour. The floor level of the middle level was thus designed as 620 m, and all of the lower level built on land with a datum ground level above 619 m should be considered as basement. This would enable an additional storey to be constructed above that part of the lowest level considered a basement. In the design, the 619 m contour passed through a balcony on the upper level. The architect did not consider the balcony to be part of the building for the determination of the number of storeys. The building certifier and the ACT government authorities agreed with the architect’s view. The design is illustrated in Figure 12. The determination of the location of the 619 m contour in the datum ground level investigation could thus be critical to whether the dwelling has two or three storeys.

7 Concluding remarks

The dispute went to court, the ACT Administrative Appeals Tribunal. Most of the initial evidence was provided by surveyors: the author for the neighbour, another surveyor for the ACT government and a third for the homeowner.

- The evidence presented by the author was largely as described in this paper. Questions were raised regarding:
- The use of LiDAR and photogrammetry intended for macro use in a micro use individual block scenario.
 - The accuracy of old data.
 - The use of plans not signed by a registered surveyor.
 - The interpolation of contours where levels had clearly been disturbed.
 - The identification of which areas were disturbed and which areas were not.
 - The definitions of datum ground level.

From the start, the Senior Member presiding over the case made it clear that in his mind, based on a site inspection, the building consisted of three stories and was hence illegal. He suggested that if others thought otherwise, they would need to change his mind, and suggested further that the parties may wish to

liaise and seek a compromise. Before the end of presenting the evidence, a compromise was reached, where the dwelling would be allowed to stand, regardless of whether legal or not, but all windows facing the neighbour were to be bricked in and a covenant inserted in the lease to the effect that no windows were to be permitted to be inserted in the wall facing the neighbour.

Unfortunately, as a consequence of the compromise, it is possible that no judgement will be made regarding the survey issues raised in the case. It seems that in the Senior Member’s view, the planning boundaries were pushed a little too far. In this case, it was shown that a Canberra homeowner and their architect were possibly stretching the planning rules beyond their legal

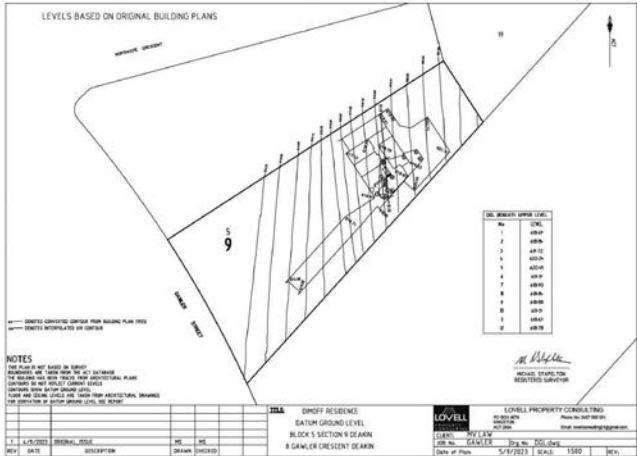


Figure 10: Datum ground level determination based on option 1.

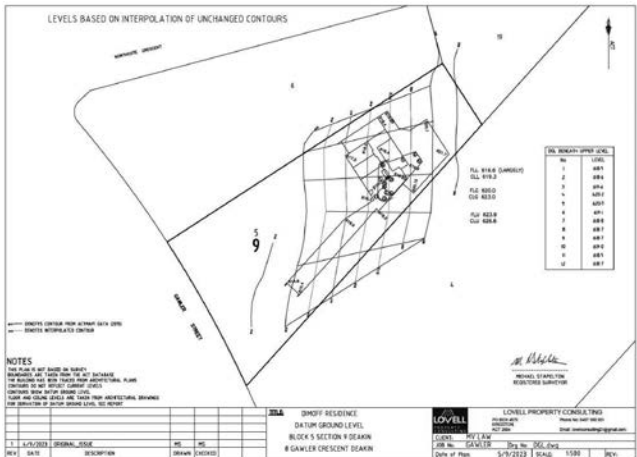


Figure 11: Datum ground level determination based on option 2.

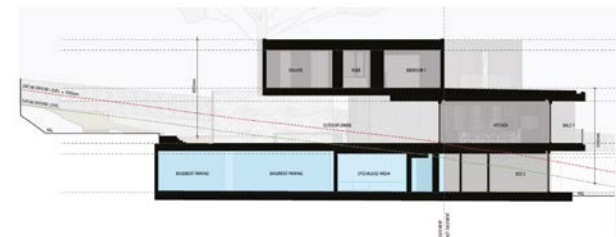


Figure 12: Example of the architect's design drawing

limits and the surveyor was critical in providing an expert opinion in this regard.

References

- ACT Government (2013) Surveyor-General of the Australian Capital Territory Guideline 12 – Datum Ground Level, <https://www.planning.act.gov.au/professionals/resources> (accessed Mar 2024).
- ACT Government (2024a) Territory Plan, <https://www.planning.act.gov.au/professionals/our-planning-system/the-territory-plan> (accessed Mar 2024).
- ACT Government (2024b) ACTmapi, <https://www.actmapi.act.gov.au/> (accessed Mar 2024).
- Australian Government (2020) National Capital Plan 1990 (December 1990), <https://www.legislation.gov.au/Details/F2020C01103> (accessed Mar 2024).
- Daly P.B. (1972) Conversion of ACT level datums to Australian Height Datum, Survey Branch, Department of the Interior, Canberra.
- Evans G. (2022) A short history of heights in the ACT, Office of the Surveyor-General and Land Information, Environment Planning and Sustainable Development Directorate, Canberra, https://www.planning.act.gov.au/__data/assets/pdf_file/0011/2329454/a-short-history-of-heights.pdf (accessed Mar 2024).
- Scrivener C.R. (1912) The contour survey of the federal capital site, *The Surveyor*, 26(5), 92-103.
- The paper was published in Proceedings of the 27th Association of Public Authority Surveyors Conference (APAS2024) Canberra, Australian Capital Territory, Australia, 18-20 March 2024. The paper is republished with author's permission.* ▴

Deep learning warm starts for trajectory optimization on the ISS

New research, published in and presented at the 2025 International Conference on Space Robotics (iSpaRo), introduces a system designed to help Astrobbee, a cube-shaped, fan-powered robot, autonomously navigate the International Space Station. The ISS is a complex environment made up of interconnected modules filled with computers, storage, wiring, and experiment hardware. This makes planning safe motion for Astrobbee far from trivial, said Somrita Banerjee, lead researcher who conducted this work as part of her Stanford PhD.

The traditional autonomous planning approaches that have gained traction on Earth are largely impractical for space-rated hardware. “The flight computers to run these algorithms are often more resource-constrained than ones on terrestrial robots. Additionally, in a space environment, uncertainty, disturbances, and safety requirements are often more demanding than in terrestrial applications,” said senior author Marco Pavone, associate professor of aeronautics and astronautics in the School of Engineering and director of Stanford’s Autonomous Systems Laboratory. Despite these challenges, the team pushed the field forward with a noteworthy space research achievement. <https://arxiv.org/pdf/2505.05588>

Civ Robotics launches AI-powered navigation system

Civ Robotics has launched a new AI-powered material distribution system for the solar industry. CivNav speeds up solar construction by streamlining logistics, efficient pile and pallet placement, and advanced planning and workflow segmentation. To use the CivNav system, the operator mounts the sensor box on their machine of choice and hops in with the CivNav tablet device in hand. It works with existing equipment; it’s compatible with any skid steer or tele-handler, and has already been installed on Bobcat, Takeuchi, Caterpillar and John Deere machines in the field. Once mounted, CivNav guides the operator where to distribute the piles, solar modules and more. The intuitive

interface enables precise placement with up to 5-cm accuracy, ensuring every plan is executed precisely.

When users combine this precise placement with GPS-enabled pile drivers, teams can skip surveying layout altogether. As the use of these GPS-enabled pile drivers increases and solar projects grow in scale, the need to cut out steps like construction staking becomes even more vital. www.civrobotics.com

Advancing DARPA autonomous space surveillance technology

The U.S. Defense Advanced Research Projects Agency (DARPA) has awarded BAE Systems’ FAST Labs™ research, development, and production organization a \$16 million Phase 2 contract for the Oversight program. It is focused on creating an autonomous system that keeps track, or maintains constant “custody,” of a large number of terrestrial assets via new satellite constellations.

The award follows the successful completion of the Phase 1 program. During Phase 1, BAE Systems’ software was integrated into a modeling and simulation environment to demonstrate a custody mission on representative satellite and sensor models. In Phase 2, BAE Systems will mature its solution algorithms and demonstrate operation with increasingly larger constellations, more complex scenarios, and higher fidelity modeling and simulation environments. The technology will be physically deployed to both tactical-edge satellites and ground stations.

The deployment of the software and algorithms developed on the Oversight program on board proliferated networked satellite constellations enables persistent surveillance at tactical timescales. Space-based coordination and data processing delivers lower latency and higher revisit rates enabling near real-time tracking. The increased scale, availability, and timeliness of information derived from space enhances warfighter situational awareness and speeds up decision making. www.baesystems.com ▴

Exploring UAS-lidar as a sampling tool for satellite-based AGB estimations in the Miombo woodland of Zambia

The findings of this study show the potential of using UAS-lidar as a sampling tool for estimating and monitoring AGB and other forest structural attributes.

Hastings Shamaoma

Department of Urban and Regional Planning,
Copperbelt University, 21692 Kitwe, Zambia.

Paxie W. Chirwa

Forest Science Postgraduate Programme,
Department of Plant and Soil Sciences,
University of Pretoria, Private Bag X20,
Hatfield, Pretoria 0028, South Africa.

Jules C. Zekeng

Department of Forest Engineering,
Advanced Teachers Training School for
Technical Education, University of Douala,
P.O. Box 1872, Douala, Cameroon.
Oliver R Tambo Africa Research Chair
Initiative (ORTARCHI), Chair of Environment
and Development, Department of
Environmental and Plant Sciences, Copperbelt
University, 21692 Kitwe, Zambia.

Able Ramoelo

Centre for Environmental Studies (CFES),
Department of Geography, Geoin-
formatics and Meteorology After CFES,
University of Pretoria, Private Bag X20,
Hatfield, Pretoria 0028, South Africa.

Andrew T. Hudak

Forestry Sciences Laboratory, USDA For-est
Service, Rocky Mountain Research Station,
1221 South Main St., Moscow, ID 83843, USA.

Ferdinand Handavu

Department of Geography, Environment and Climate
Change, Mukuba University, 20382 Kitwe, Zambia.

Stephen Syampungani

Forest Science Postgraduate Programme,
Department of Plant and Soil Sciences, University
of Pretoria, Private Bag X20, Hatfield, Pretoria
0028, South Africa.
Oliver R Tambo Africa Research Chair
Initiative (ORTARCHI), Chair of Environment
and Development, Department of
Environmental and Plant Sciences, Copperbelt
University, 21692 Kitwe, Zambia.

Abstract

To date, only a limited number of studies have utilized remote sensing imagery to estimate aboveground biomass (AGB) in the Miombo ecoregion using wall-to-wall medium resolution optical satellite imagery (Sentinel-2 and Landsat), localized airborne light detection and ranging (lidar), or localized unmanned aerial systems (UAS) images. On the one hand, the optical satellite imagery is suitable for wall-to-wall coverage, but the AGB estimates based on such imagery lack precision for local or stand-level sustainable forest management and international reporting mechanisms. On the other hand, the AGB estimates based on airborne lidar and UAS imagery have the precision required for sustainable forest management at a local level and international reporting requirements but lack capacity for wall-to-wall coverage. Therefore, the main aim of this study was

to investigate the use of UAS-lidar as a sampling tool for satellite-based AGB estimation in the Miombo woodlands of Zambia. In order to bridge the spatial data gap, this study employed a two-phase sampling approach, utilizing Sentinel-2 imagery, partial-coverage UAS-lidar data, and field plot data to estimate AGB in the 8094-hectare Miengwe Forest, Miombo Woodlands, Zambia, where UAS-lidar estimated AGB was used as reference data for estimating AGB using Sentinel-2 image metrics. The findings showed that utilizing UAS-lidar as reference data for predicting AGB using Sentinel-2 image metrics yielded superior results ($\text{Adj-R}^2 = 0.70$, $\text{RMSE} = 27.97$) than using direct field estimated AGB and Sentinel-2 image metrics ($\text{R}^2 = 0.55$, $\text{RMSE} = 38.10$). The quality of AGB estimates obtained from this approach, coupled with the ongoing advancement and cost-cutting of UAS-lidar technology as well as the continuous availability of wall-to-wall optical imagery such as Sentinel-2, provides much-needed direction for future forest structural attribute estimation for efficient management of the Miombo woodlands.

Introduction

Sustainable management and carbon accounting of forests require accurate up-to-date vegetation structural data, often covering extensive areas that are too huge

to capture, process, and manage by manual methods [1–6]. Typically, above ground biomass (AGB) in the Miombo woodlands is determined using destructive harvesting procedures, for building allometric equations based on the observed data from these cut trees, such as diameter at breast height (DBH), tree height, and wood density [7–9]. Nevertheless, the application of these allometric equations on extensive forest regions can pose challenges in terms of time, cost, and feasibility due to the difficulty in obtaining field measurement input parameters in remote terrains. Consequently, the AGB for most of vegetation formations in many parts of the African savannas, Miombo woodlands inclusive remains poorly understood.

Remote sensing has made it possible to measure vegetation structure across vast areas in an efficient and repetitive manner [10, 11]. The application of remote sensing methods in estimating AGB in the Miombo woodlands [12–18] is becoming common. Most of these studies employ statistical models where field estimates of AGB are regressed against metrics generated from corresponding remote sensing data, followed by extrapolation of resulting models to the entire study area. The studies that have employed remote sensing imagery for estimation of AGB in the Miombo ecoregion so far have done it at two levels of abstraction, namely: (i) wall-to-wall estimation of AGB; and (ii) local or stand-level estimations. The wall-to-wall category includes, the use of atmospherically resistant vegetation indices (ARVI) and normalized difference vegetation indices (NDVI) derived from Landsat imagery to assess forest cover, stocking and above-ground tree biomass dynamics in the Miombo woodlands of Tanzania [14]. In another study, Halperin et al. [12, 19] estimated AGB in Nyimba district, Miombo woodlands, Zambia, using National Forest Inventory (NFI) data, estimated canopy cover, environmental data, disturbance data, and Landsat 8 OLI satellite imagery. The medium resolution imagery (Landsat) utilized in Kashindye et al. [14] and Halperin et al. [12, 19] are suitable for wall-to-wall coverage, but the AGB estimates

based on such imagery lack precision for local or stand-level sustainable forest management, as well as international reporting mechanisms [20] such as reducing emissions from Deforestation and Forest Degradation, plus forest conservation, sustainable management of forests and enhancement of carbon stocks (REDD+) and Monitoring, Reporting and Verification (MRV), which offers monetary rewards to developing countries for forest conservation, and the execution of ecologically sound forest management based on national carbon stocks reported to the United Nations Framework Convention on Climate Change, UNFCCC [2, 21].

At a local level, Mauya et al. [16] employed airborne light detection and ranging (lidar) data to estimate AGB in the Miombo woodlands of Liwale district, Tanzania. Another study by Kachamba et al. [13], utilized unmanned aerial systems (UAS) image-based point clouds to estimate AGB in the Miombo woodlands, Muyobe forest, and Mzimba District in northern Malawi. The AGB data estimates by Mauya et al. [16] and Kachamba et al. [13] have the precision required for sustainable forest management at a local level and international reporting requirements but lack capacity for wall-to-wall coverage. Furthermore, apart from the limited area coverage inherent in the UAS imagery approach employed in Kachamba et al. [13], the imagery requires huge storage space and high processing speeds [22, 23] that are too demanding and still challenging for wall-to-wall estimations of AGB over a large area. As a result, the two levels of abstraction must be linked in order to get wall-to-wall AGB estimates with the accuracy necessary for local sustainable forest management and international carbon reporting requirements [2, 21].

With regard to bridging the spatial gap between wall-to-wall satellite imagery and detailed airborne and UAS imagery, some studies have proposed a two-phase sampling design where areas covered by UAS or airborne imagery are sampled via field plots and areas covered by wall-to-wall satellite images are sampled using UAS or airborne imagery, for example,

lidar sampling [24–28] and UAS imagery sampling [29, 30]. These strategies have demonstrated tremendous potential to reduce field plot installation costs and improve wall-to-wall AGB estimate accuracy, which could provide solutions for forest data collection in forest inventory-plagued regions such as the Miombo ecoregion. A study by Wulder et al. [31] presented a complete review of employing lidar sampling to allow large-area forest characterizations, in which lidar samples were utilized in a way comparable to field samples. However, their review focused on airborne, which are still expensive to acquire in the Miombo region. UAS provide a more flexible and affordable sampling platform for use in conjunction with wall-to-wall satellite imagery, as demonstrated in recent studies [28, 30, 32].

In a pioneering study for UAS-based sampling, Puliti et al. [30] used UAS photogrammetric point clouds as a sampling tool, together with a limited sample of field data and wall-to-wall Sentinel-2 images, to estimate growing stock volume in a 7330 hectare forest area in Norway using a hierarchical model-based inference and reported this approach to be cost-effective for large scale forest resource assessments. However, UAS photogrammetric point clouds have been reported to have challenges in capturing the vertical vegetation structure that are required for estimating AGB in denser forest environments [22, 33]. In a related study, Wang et al. [32] used a lidar sensor mounted on a UAS platform (UAS-lidar) partial coverage data as a link between field plot data and wall-to-wall Sentinel-2 imagery to estimate man-grove forests AGB in Hainan Island, China. Apart from lowering field sampling costs, their research observed that their method produced better AGB estimations ($R^2 = 0.62$; $rRMSE = 35.41\%$) than the usual method, which directly correlates field plots to Sentinel-2 data ($R^2 = 0.0.52$; $rRMSE = 39.88\%$).

This paper proposes a two-phase sampling technique for low-cost, large-scale AGB estimates for the Miombo ecoregion by

capitalizing on publicly-available Sentinel-2 satellite images and inexpensive UAS-lidar data. In order to achieve this, the specific objectives were: (i) to identify suitable UAS-lidar metrics and Sentinel-2 metrics for estimating AGB in the Zambian Miombo; (ii) to identify the optimal prediction model for mapping AGB; (iii) to assess if UAS-lidar-estimated AGB can replace field-estimated AGB as reference data; and (iv) to compare the findings of direct field plots to Sentinel-2 AGB estimations from utilizing field plots to UAS-Lidar and UAS-lidar to Sentinel-2 in a two-phase sampling strategy.

Materials and method

Study area

The research was conducted in Miengwe Forest Reserve Number 36, Masaiti District, Copperbelt Province, Zambia (Fig. 1). The forest reserve is situated

approximately 17 km from the Ndola-Lusaka highway and 90 km south-west of the Ndola city center. The 8,094-ha Miengwe Forest Reserve is located between 13°24'05"S and 28°49'00"E. The region receives an average of 1200 mm of rainfall annually and experiences three distinct sea-sons: hot dry (September–November), rainy (December–March), and cold dry (April–August) [7]. The most prevalent soil form is residual lateritic soil, which consists primarily of silty clays and sediments. The area is within the Wet Miombo region and is characterized by the dominance of the families of Papilionaceae and Fabaceae. The dominant genera and species are *Brachystegia* (*Brachystegia spiciformis* and *Brachystegia longifolia*), *Julbernardia* (*Julbernardia globiflora* and *Julbernardia pan-iculata*), and *Isoberlinia* (*Isoberlinia angolensis*).

Field sample plots

To ensure that field sample plots,

UAS-lidar data, and Sentinel-2 data corresponded in the two-phase sampling approach [34], the Sentinel-2 image covering the study area was resampled to 20 m spatial resolution and used to generate a 20 × 20 m grid framework that served as the foundation for both field and UAS-lidar sampling (Fig. 2). The study area was divided into ten UAS lidar blocks ranging in size from 30 to 50 hectares, which were selected based on the vegetation coverage, accessibility, and availability of a UAS launch site as determined by visual interpretation of Google Earth images and field assessment. In each of the UAS-lidar blocks, ten to twelve circular sample plots of 10 m radius were established at 250 m spacing at the centre of the 20 × 20 m Sentinel-2 grid framework, at least 50 m distant from the block border. These plots were designed to align with the 20 × 20 m grids that were used for extracting UAS-lidar metrics. The LT700H real time kinematic RTK

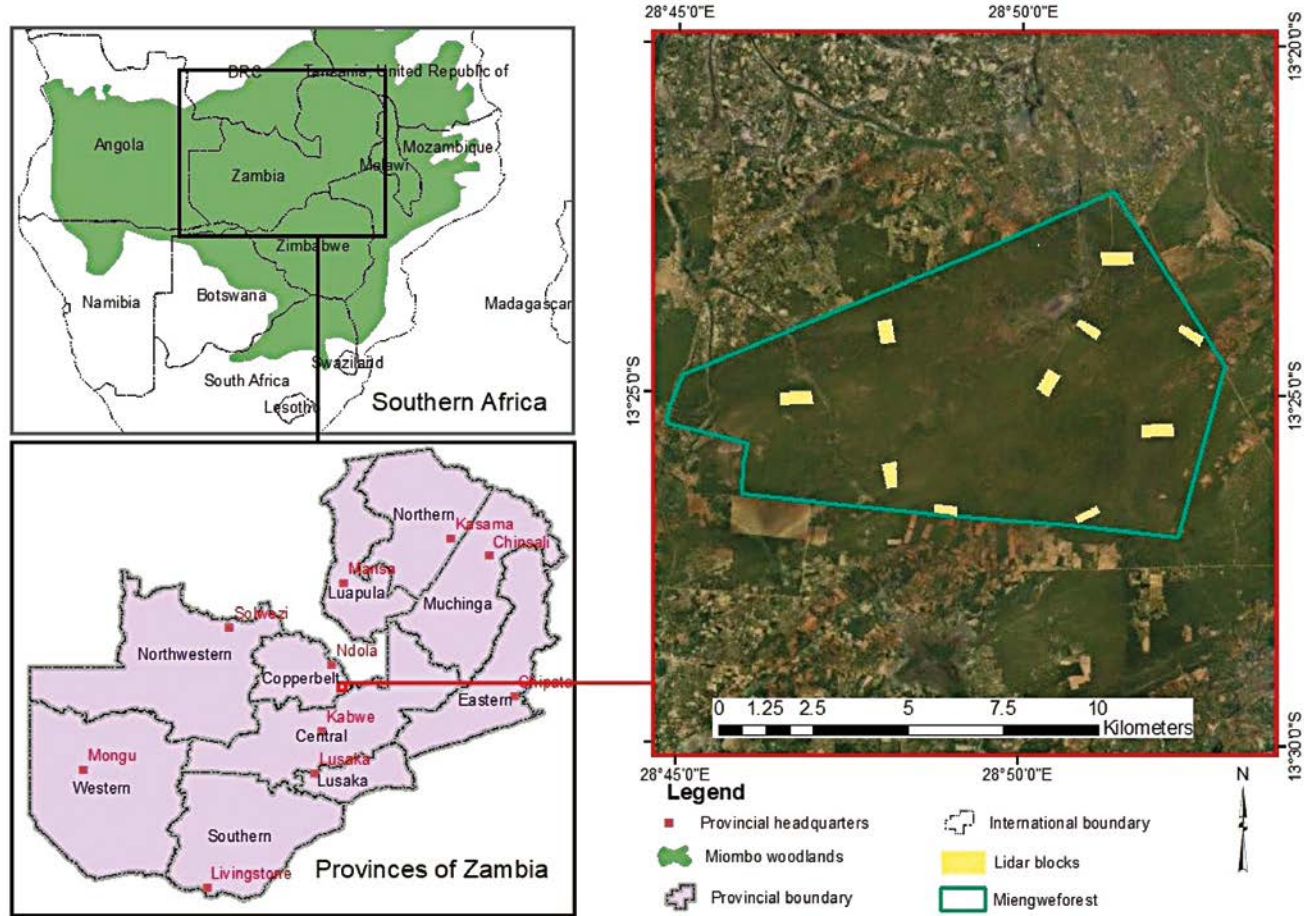


Fig. 1 Location of study area

(Shanghai Huace Navigation Technology Limited, China) Global Navigation Satellite Systems (GNSS) receiver was used to precisely locate the centers of these plots on the ground to within a few centimeters. The DBH, tree height, and species names of trees with DBH more than 5 cm were recorded in each of the sample plots. Allometric equations proposed by Handavu et al. [7] were used to estimate AGB at the plot level.

Collecting and pre-processing data from UAS-lidar

Using a T-Drone M1200 quadcopter equipped with a gAirHawk GS-100C UAS-lidar scanning system, we collected the raw UAV-lidar point clouds between November 10th and 12th, 2021. The Livox Avia sensor on the GS-100C UAS-lidar operates at 200 HZ and can provide up to 720,000 points/sec in triple echo. The mission was planned using the open-source program Mission Planner, which was also used to track the aircraft in real-time and monitor its flight characteristics. UAS-lidar data were collected at an altitude of 80 m, a speed of 5 m per second, and a swath width of 42 m. A GNSS ground base station was used as a reference for subsequent UAS-lidar data post-processing.

The unprocessed UAS-lidar data downloaded from the GS-100C comprised raw lidar points, UAS inertia measurement unit data, UAS GNSS data, and raw

photogrammetry imagery (used for colourising the point cloud). The raw UAS-lidar data and raw GNSS data from the ground GNSS base station were first processed in gAirhawk 5.0 version software (Geosun Navigation Technology Lim-ited, Wuhan, China), where lidar data, IMU data, and GNSS base data were integrated to process the flight trajectory and generate georeferenced UAS-lidar point cloud data in las format. The UAS-lidar point cloud data in las format underwent further processing in Lidar360 version 5.4.3.0 software (GreenValley International, California, CA, USA), which included: (i) denoising the lidar point cloud using an outlier reduction method; (ii) classification of point clouds into either ground or non-ground using an enhanced version of the progressive triangulated irregular network (TIN) densification filter method [35]; and (iii) normalizing point clouds by subtracting the elevation of each point from the DTM that was generated using the inverse distance weighting (IDW) interpolation technique. The normalized points were used as input for extracting UAS-lidar metrics which were used for the subsequent modelling.

Sentinel-2 data collection and pre-processing

There were no cloud-free images for November 2021 to coincide with the lidar data collection period, so Sentinel-2 images with less than 5% cloud

cover captured in November 2022, which reflected the closest state to the time lidar data was collected, were downloaded from the open access European Space Agency [36]. The Sentinel Application Platform (SNAP) and ArcGIS Desktop Version 10.7.1 [37] software were used to pre-process the raw Sentinel-2 imagery. The Sen2Cor atmospheric correlation processor (version 2.5.5) was used to do atmospheric correction to create Level2A bottom-of-atmosphere reflectance data. Three visible bands [Blue (B2), Green (B3), and Red (B4)], three red edge bands [Red Edge 1 (B5), Red Edge 2 (B6), and Red Edge 3 (B7)], two near infrared bands (B8) and Narrow Near Infrared (B8a)), and two shortwave bands [Shortwave 2 (B12) and Shortwave 3 (B13)] were used in the Sentinel-2 image composite. Bands 1, 9, and 10 were removed because they were dedicated to atmospheric correction and had coarse resolution of 60 m. All adopted bands were resampled to 20 m resolution using the nearest neighbor approach in ArcGIS to match our sampling strategy [28, 38, 39]. Finally, subsets of all generated sentinel-2 imagery products were clipped to the size of the study area.

Extraction of AGB predictors

The UAS-lidar metrics were extracted in Lidar360 software based on polygons generated from a 20×20 m resampled Sentinel-2 grid framework (Fig. 2). We generated a total of 37 UAS-lidar metrics at the plot level (Table 1). The 20×20 m grid framework was generated based on the re-sampled Sentinel-2 using the “create fishnet tool” in ArcToolbox, implemented in ArcGIS Desktop software, which includes an option for generating points inside each grid. The points inside each grid served as the basis for extracting Sentinel-2 image metrics for estimating the AGB for the study area.

Acquiring Sentinel-2 metrics

Prior experience [38, 39] in estimating AGB using Sentinel-2 imagery influenced the choice of relevant bands as well as the derived vegetation indices (VI) and biophysical variables (BV) in this

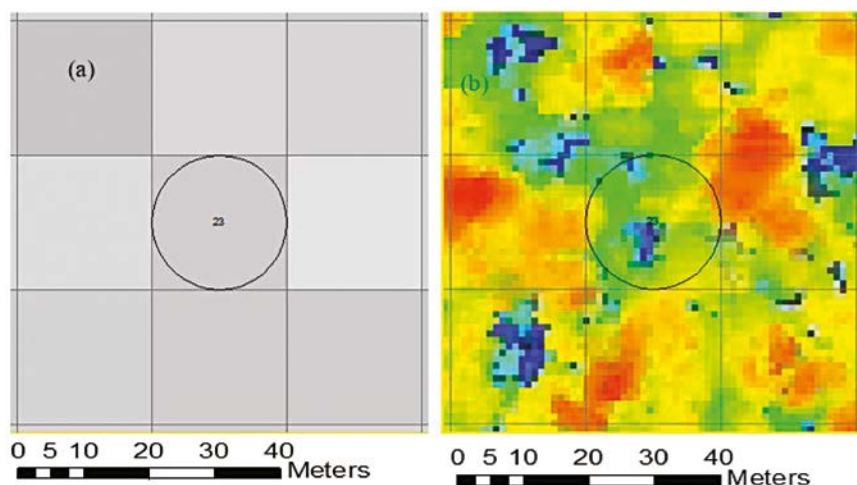


Fig. 2 Sample plot and grid framework overlaid on: a Sentinel-2 image and b lidar point cloud

work (Table 2). In addition, normalized difference fraction index (NDFI), an index that has been widely used to monitor forest disturbances in the tropics [40–42] was calculated. It is based on spectral unmixing, which is the breakdown of the spectral signature of a mixed pixel into proportions of endmembers (pure

spectra) [43]. Using this approach, Souza et al. [41] employed a linear mixture model to decompose field data on cleared, selectively logged, and undisturbed Amazon forests into proportions of soil, shade, green vegetation (GV), and non-photosynthetic vegetation (NPV). Dense forests revealed high GV and

low soil, NPV, and shade percentages. Cleared and thinned forests exhibited greater canopy shade and GV than non-disturbed forests. The NDFI was adopted in this study because it emphasizes the difference between forest and non-forest pixels [40], which is crucial for estimating AGB. The NDFI

Table 1 UAS-lidar metrics

Lidar metrics	Description
Percentile heights (H1, H5, H10, H20, H25, H30, H40, H50, H60, H70, H75, H80, H90, H95, H99)	The percentile of the canopy height distributions (1st, 5th, 10th, 20th, 25th, 30th, 40th, 50th, 60th, 70th, 75th, 80th, 90th, 95th and 99th) of first returns
Canopy return density (D1, D2, D3, D4, D5, D6, D7, D8, D9)	The proportion of points above the quantiles (10th, 20th, 30th, 40th, 50th and 60th, 70th, 80th and 90th) to total number of points
Variance of height (Hvar)	The variance of the heights of all points
Maximum height (Hmax)	Maximum of return heights above 2 m
Coefficient of variation of heights (Hcv)	Variation of heights of lidar returns above 2 m
Hskew	Skewness of height
Hmd	The median of absolute deviation of heights
Hkurtosis	The kurtosis of the heights of all points
Hstd	Standard deviation of height
Hmean	Mean height above ground of all first returns
Canopy relief ratio (CRR)	Mean height returns minus the minimum height divided by the maximum height minus the minimum height
Canopy cover (CC) above 2 m	Percentile of first returns above 2 m
Gap fraction (GF)	An indication how much of the sky is visible from beneath a plant canopy
Leaf area index (LAI)	Half of the surface area of all leaves per unit ground area

Table 2 Selected multispectral bands, VI, and BF from Sentinel-2 images

Bands	Description	Central wave length (nm)
B2	Blue	490
B3	Green	560
B4	Red	665
B5	Vegetation red edge	705
B6	Vegetation red edge	740
B7	Vegetation red edge	783
B8	Near infrared (NIR)	842
B11	Short wave infrared (SWIR)	1610
B12	Shortwave infrared (SWIR)	2190
Vegetation indices	Description (reference)	Equation
NDVI	Normalized Difference Vegetation Index [76]	$NDVI = \frac{B8 - B4}{B8 + B4}$
EVI	Enhanced vegetation index [76]	$EVI = 2.5 \times \frac{(B8 - B4)}{(B8 + 6 \times B4 - 7.5 \times B2 + 1)}$
SAVI	Soil adjusted vegetation index [76]	$SAVI = \frac{B8 - B4}{B8 + B4 + L} \times (1 + L)$
RENDVI_705	Red-edge normalized difference vegetation index [76]	$RENDVI = \frac{B8 - B5}{B8 + B5}$
NBRI	Normalized Burn Ratio Index [60]	$NBRI = \frac{B8 - B12}{B8 + B12}$
GNDVI	Green Normalized Difference Vegetation Index [77]	$GNDVI = \frac{B8 - B3}{B8 + B3}$
Biophysical variables	Description (reference)	
LAI	Leaf area index [39]	
FAPAR	Fraction of absorbed photosynthetically active radiation [39]	
FCOVER	Fraction of vegetation cover [39]	
CAB	Chlorophyll content in the leaf [39]	

was calculated using Eq. 1 and GV_{shade} is the shade-normalised GV fraction given by Eq. 2 [41].

$$NDFI = \frac{GV_{shade} - (NPV + Soil)}{GV_{shade} + (NPV + Soil)} \quad (1)$$

$$GV_{shade} = \frac{GV}{1 + Shade} \quad (2)$$

NDFI is the ratio of the GV, NPV, soil, and shade end-member fractions, with the resulting NDFI values ranging from -1 to 1. In the present study, the calculation of the NDFI was implemented within the System for Earth Observation Data Access, Processing, and Analysis for Land Monitoring (SEPAL) cloud application [44]. Subsequently, the final suitable metrics for the study were arrived at after undergoing a variable selection process.

Predicting AGB

The multi-linear regression (MLR) approach was employed to predict AGB in this study because of its simplicity and ability to handle dependencies on or correlations between the predictor variables [26, 45]. A two-phase sampling approach was utilized to estimate the AGB for the Miengwe forest. The first phase involved creating the ground plot to UAS-lidar relationship and estimating AGB in the blocks covered by UAS-lidar. The UAS-lidar blocks were selected based on accessibility and availability of a UAS launch site and did not follow a strict north-south orientation. Since the UAS-lidar blocks did not match the orientation of the Sentinel-2-generated grid framework, the grid cells in the UAS-lidar block's margins, covering only a fraction of the 400-m square grid, were removed. We estimated the AGB for a total of 4248 grid cells covering all the 10 UAS-lidar blocks in the study area, representing about 2.5% of the total Miengwe forest area. The estimated AGB of the UAS-lidar blocks were used as reference points in the subsequent estimation of AGB in areas covered by Sentinel-2 imagery for the rest of the study area.

In the second phase, a relationship was established between the UAS-lidar predicted AGB (response variable) and wall-to-wall Sentinel-2 image metrics (Table 2) as predictor variables to estimate the AGB for the entire study area using MLR technique. Seven hundred random (700) points were generated within the 10 UAS-lidar blocks using the create random points tool implemented in ArcGIS Desktop Version 10.7.1. The 700 random samples of UAS-lidar estimated AGB grid cells served as training data for estimating AGB for the whole study area using Sentinel-2 image metrics.

We also predicted the AGB for the Miengwe forest using the direct relationship between ground plots and Sentinel-2 imagery metrics, which allowed us to assess whether or not the use of UAS-lidar as a bridging sampling tool between the two was beneficial. The UAS-lidar to Sentinel-2 estimated AGB was later compared with the one obtained directly the ground points to Sentinel-2 metrics estimated AGB.

The MLR modeling approach

The first stage of variable selection involved using Pearson's correlation coefficient (r) to evaluate the association between the dependent variable and the independent variables to ensure model parsimony and eliminate overfitting by removing predictor variables with high levels of correlation with each other ($r > 0.85$). The best subsets regression approach built in Minitab Version 21.1.1 [46] was used to identify the best performing model and variables from a set of selected variables. As a model selection method, best subsets regression involves trying out every conceivable collection of predictor variables and picking the one that performs the best statistically [47]. The best model is chosen based on different criteria including: highest adjusted-R² and predicted-R² as well as the lowest values for Mallows Cp, Akaike's Information Criterion corrected (AICc), and Bayesian information criterion (BIC). In our case the model with lowest AICc was considered to be the best as it has been proved to perform well for smaller samples in prior studies [48, 49]. Finally, the best MLR model was used to predict the AGB.

To compare the predicted values with the observed values (AGB values acquired from lidar), three accuracy assessment indicators employed in Liu et al. [50] were utilized. The developed MLR models were tested using k-fold cross validation to determine their accuracy. The idea behind this method is to randomly divide the data into k groups or folds where each member is nearly the same size. When doing k-fold cross-validation, each fold is treated as its own validation set. We choose $k = 10$ because this number has been widely used and empirically proved to provide non-biased and rather stable estimates of the test error rate. Ten subsets of the original dataset are created and used for tenfold cross-validation. Each fold uses 9 of the 10 subsets for training and the remaining 1 for testing the accuracy of the learnt model on the validation set. Each subgroup will undergo the validation procedure many times. Finally, we utilized the aforementioned equations to calculate cross-validated RMSE from a table containing all of the folds' predicted values.

Results

Variables selection

In this study, three models were developed to predict AGB in two phases: Model 1, represented by Eq. 3, utilized the correlation between field estimated AGB and UAS-lidar metrics. Model 2, represented by Eq. 4, utilized the correlation between UAS-lidar estimated AGB and Sentinel-2 metrics. Model 3, represented by Eq. 5, was developed by utilizing the direct correlation between field estimated AGB and Sentinel-2 image metrics for the purpose of comparing with model 2. Since the processes for models 1–3 are similar, we only show the variable selection process for model 1. The variable CC emerged as the primary predictor in all ten models identified in the best subsets approach, indicating its significant influence (Table 3). Hcv and H80 were also shown to be influential predictors, since they

were picked in seven out of the ten models. Overall, height related metrics dominated the list of selected lidar metrics.

The model of four predictor variables was chosen to be the best model because it produced the highest predicted R^2 and lowest AICc (Bolded in Table 3), and was less complicated compared to the model of six predictor variables. After implementation of the chosen model, it resulted in model 1, Eq. 3. This selection procedure was repeated in phase two for estimating UAS-lidar-derived AGB using Sentinel-2 metrics and resulted in model 2, Eq. 4 (Table 4). The same procedure was applied to directly estimate AGB using the relationship between field-estimated AGB and Sentinel-2 metrics, resulting in model 3, Eq. 5

$$\ln(AGB) = 1.68CC + 0.08H80 + 5.32D20 - 2.97Hcv + 0.20 \tag{3}$$

$$\ln(AGB) = 4.18NDFI + 0.24LAI + 5.98NBRI - 14.53B06 - 8.49B12 + 3.15B11 + 2.05 \tag{4}$$

$$AGB = 2778B11 + 1084GNDVI + 59.1LAI - 1171 \tag{5}$$

AGB estimation at phase one

Estimation of AGB by applying the relationship between field estimated AGB and UAS-lidar metrics using model 1 explained 90% of the variance of AGB, RMSE of 17.70 Mg/ha and a bias of 3.79 Mg/ha (Table 5) and Fig. 3a, indicating that the model successfully predicted the AGB.

AGB estimation at phase two

In phase 2, UAS-lidar prediction of AGB from phase one were used as sample data for predicting AGB using the relationship with Sentinel-2 variables (Eq. 4, model 2) and was able to explain 79% of the variance of AGB for the entire Miengwe forest. Additionally, model 2 was used to generate the AGM map at 20 m resolution for the Miengwe forest (Fig. 4). The RMSE of 27.97 Mg/ha and bias of 3.94 Mg/ha was achieved (Table 4) and Fig. 3b. With a cross-validated predicted $R^2 = 0.64$, this demonstrated potential for applying UAS-lidar sampling when

Table 3 Candidate MLR Models for Field estimated AGB prediction using UAS-lidar metrics (see Table 1 for UAS-lidar metrics description)

Vars	R ²	adj-R ²	pred-R ²	Cp	RMSE	AICc	BIC	CC	Haad	H20	H30	H80	H99	Hcv	D10	D20	D30	D70
1	0.66	0.65	0.56	37.7	0.19441	28.629	27.312	X										
2	0.79	0.77	0.53	20	0.16265	21.062	20.189	X		X								
3	0.84	0.82	0.74	3.9	0.12312	8.524	7.814	X		X	X							
4	0.89	0.87	0.82	1.6	0.10209	0.995	0.122	X	X	X	X							
5	0.90	0.87	0.82	0	0.10318	4.08	2.664	X	X	X	X							X
6	0.90	0.87	0.79	1.5	0.10399	7.401	4.995	X	X	X	X				X	X		
7	0.90	0.87	0.77	3.2	0.10564	11.59	7.663	X	X	X	X			X	X	X		
8	0.90	0.86	0.76	5.1	0.10835	16.841	10.755	X	X	X	X			X	X	X	X	
9	0.90	0.85	0.67	7	0.11127	22.837	13.819	X	X	X	X	X	X	X		X	X	
10	0.90	0.84	0.54	9	0.11481	29.93	17.027	X	X	X	X	X	X	X		X	X	X

X: selected variable, bold values: selected model

Table 4 Candidate MLR Models for UAS-lidar estimated AGB prediction using Sentinel-2 metrics (see Table 2 for Sentinel-2 metrics description)

Vars	R ²	adj-R ²	pred-R ²	Cp	RMSE	AICc	BIC	NDFI	B02	NBRI	B06	B11	B07	B05	B12	B04	LAI
1	46.3	46.3	45.2	268.2	0.66021	1493.583	1507.379				X						
2	56.1	56.0	54.8	87.0	0.59750	1346.480	1364.864	X			X						
3	58.8	58.7	57.3	38.1	0.57911	1301.127	1324.092	X			X	X					
4	59.7	59.5	58.1	23.2	0.57311	1286.692	1314.234	X			X	X			X		
5	65.3	65.1	62.8	13.8	0.56914	1277.416	1309.529	X			X		X		X		X
6	78.7	70.4	63.9	9.5	0.56615	1273.136	1309.914	X		X	X		X		X		X
7	78.8	70.4	63.9	9.4	0.56671	1273.144	1314.382	X			X	X	X		X		X
8	78.9	70.5	63.8	9.4	0.56633	1273.184	1318.977	X	X	X	X		X	X	X		X
9	79.0	70.5	63.7	9.0	0.56579	1272.816	1323.157	X	X	X	X	X	X	X	X		X
10	79.0	70.5	63.3	11.0	0.56617	1274.856	1329.741	X	X	X	X	X	X	X	X	X	X

X: selected variable, bold values: selected model

Table 5 Summaries of used models

Model	R ²	adj-R ²	Pred-R ²	RMSE (Mg/ha)	rRMSE%	Bias (Mg/ha)
Ground—UAS-lidar	0.90	0.87	0.81	17.70	14.38	3.79
UAS-lidar—Sentinel-2	0.79	0.70	0.64	27.97	28.89	3.94
Ground—Sentinel-2	0.62	0.55	0.46	38.10	37.54	6.19

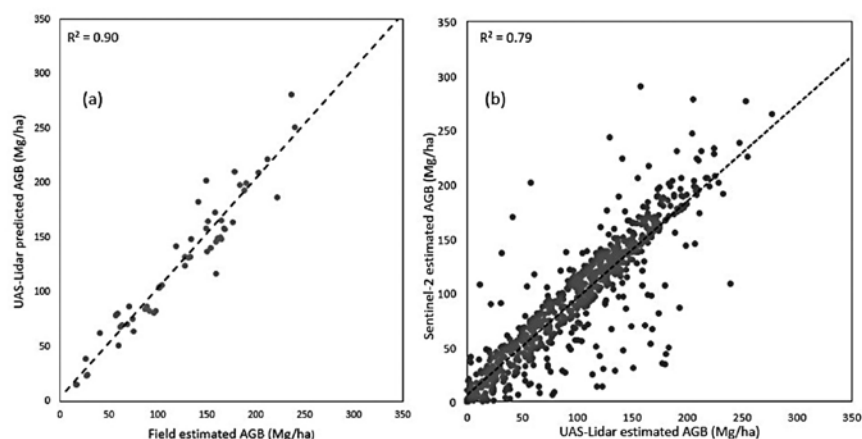


Fig. 3 Scatter plots showing estimation of above ground biomass: a Ground to UAS-lidar model and b UAS-lidar to Sentinel-2 model

estimating AGB using Sentinel-2 imagery, contrasting it with what was determined using usual direct ground sampling to Sentinel-2 metrics, explaining only 62% of the variance of AGB across the Miengwe forest and a cross-validated predicted $R^2 = 0.46$ Table 5 and Fig. 5). The UAS-lidar-Sentinel-2 model exhibited a bias of 3.94 Mg/ha, which was only slightly higher than the bias of 3.79 Mg/ha in the Ground-UAS-lidar model, showing a good match between Sentinel-2 and UAS-lidar data and validating the use of UAS-lidar sampling.

Discussion

Accurately estimating AGB across extensive forest areas presents a significant challenge. Currently, AGB estimates for the majority of the vegetation formations of the Miombo woodland remain unknown, and corresponding AGB maps for these areas are unavailable. The present study presents the approach for producing an AGB map (Fig. 3) for Miombo woodland through utilization of a two-phase UAS-lidar sampling methodology that lever-ages the combined advantages of field plots, UAS-lidar technology, and Sentinel-2 imagery.

Choosing the optimal predictors for estimating the AGB

The process of variable selection was conducted in order to identify the optimal predictors for accurately estimating the AGB across all phases. The first phase involved selecting best predictors for estimating AGB using the relationship between field estimated AGB and UAS-lidar derived metrics. The second phase involved selecting best predictors for estimating AGB using the relationship between UAS-lidar metrics estimated AGB and metrics derived from Sentinel-2 imagery. The third and final phase was to select the best Sentinel-2 metrics for predicting AGB using the relationship between AGB estimated through field observations and Sentinel-2 image metrics.

In phase 1, the most important predictors for AGB were a set of metrics associated with height, density, and canopy cover.

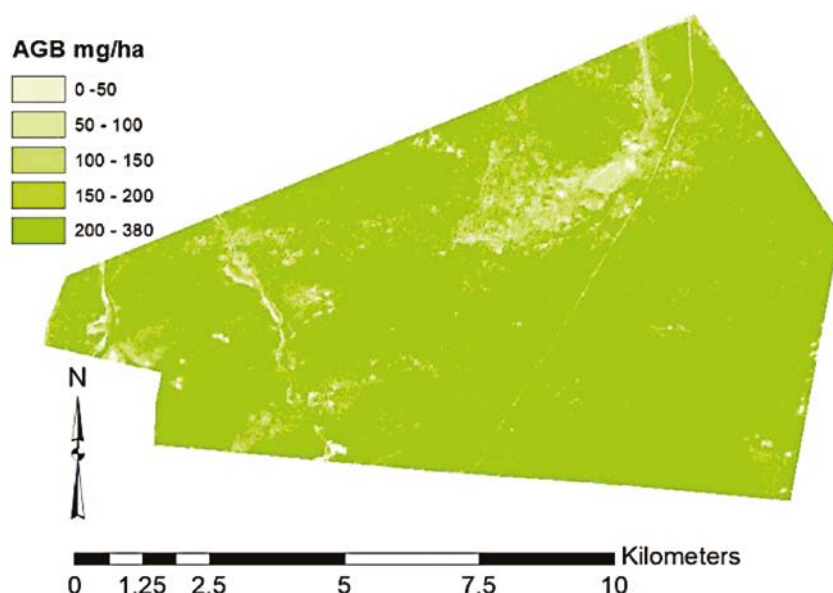


Fig. 4 Biomass map for Miengwe forest at 20 m resolution

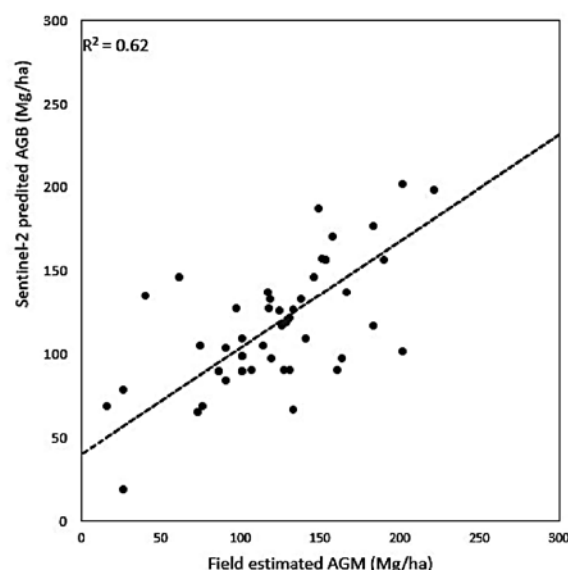


Fig. 5 Scatter plots showing estimation of above ground biomass using ground to Sentinel-2 model

CC was the most important predictor selected in all the 10 models for predicting AGB, followed by Hcv and H80, which were selected in 7 of the 10 models (Table 3). This accords with UAS-lidar metrics selected in previous studies elsewhere, for example, height percentiles [50–52], canopy cover [50, 51], canopy density [51] and coefficient of variation for heights [50, 53, 54] for estimating AGB. Several previous studies [50, 55, 56] have demonstrated the utility of Hmean as a predictor for estimating aboveground biomass (AGB).

However, in our study, it was seen that Hmean exhibited a strong correlation with other predictors, and as a result, it was excluded from further consideration. The differences in the selected predictors can be attributed to variation in metric selection algorithms, modelling approach and variation in forest structure and composition [57–59].

For phase 2, the best Sentinel-2 image metrics predictors for estimating AGB were vegetation indices (NDFI and NBRI), the red-edge band (B6), SWIR bands (B11 and B12) and the biophysical variable LAI. The vegetation indices (NDFI and NBRI) and red-edge bands (B7 and B6) were strong for models with fewer predictor variables (models 1–3, Table 4) because they are known to be good for separating vegetated from non-vegetated areas [39–41, 60], which is critical for AGB estimation. The red edge band lies at a specific wavelength that fluctuates swiftly at the convergence of the near-infrared and red spectral bands [57]. This band is highly responsive to subtle changes in both the structure of the plant canopy and the chlorophyll content. Consequently, it is regarded as having the capacity to mitigate saturation effects and improve estimation of AGB, supporting works by other researchers (e.g. [61]). Furthermore, this supports an assertion by Adam et al. [62] that vegetation indices possess the ability to mitigate the effects of shadows and environmental factors on reflectance, thereby enhancing their correlation with AGB. The addition of the SWIR bands and the biophysical variable

LAI resulted in improved models (models 5–10, Table 4). This finding is consistent with previous studies conducted by Dang et al. [63] in Yok Don National Park, Vietnam, Mauya and Madundo [38] in tropical montane forests of Tanzania, and Moradi et al. [64] in Zagros oak forests in Iran, who reported a high correlation between AGB and red, red-edge, NIR and SWIR bands and vegetation indices that are derived from them.

B11, NDFI, and LAI were the selected predictors (Eq. 5) for directly calculating AGB using field-estimated AGB and Sentinel-2 measurements. This was consistent with the results of Muhe and Argaw [39], who employed Sentinel-2 metrics to estimate AGB in a tropical afro-montane forest in Ethiopia. However, unlike Muhe and Argaw [39], Sentinel-2-derived biophysical variables were observed to be significantly correlated with each other, and just LAI was utilized to develop the model as opposed to the three biophysical variables applied in Muhe and Argaw [39]. Sentinel-2 derived products (indices and biophysical factors) were added instead of raw Sentinel-2 bands only since they were shown to enhance AGB estimates in previous research [39, 65]. The NDFI was a strong predictor in both models 2 and 3. This is not surprising because this index has been observed to be good at discriminating vegetated from non-vegetated areas [40, 41]. In addition to selecting a suitable regression model, the variable selection strategy approach was crucial to lowering the feature dimension, minimizing information redundancy, and enhancing modeling efficiency [47].

Identify the optimal prediction model for mapping AGB

After choosing the most important predictors for estimating AGB at the two phases, best subsets regression [47], was used to come up with the best models for predicting AGB at all phases (Tables 3 and 4). Our criteria were based on the model with the highest prediction accuracy (pred-R²) as well as the lowest AICc, BIC and Mallows Cp, followed by

the model with the fewest predictors, in that order. However, the most important consideration in selecting the optimal model was checking to see whether it contains variables that are consistent with ecological reasoning and have been shown to be strong AGB predictors in the literature [66]. The model included height metrics including the lower, middle, and upper percentiles, thereby offering data on the distribution of tree heights, as well as metrics for canopy cover and density, thus yielding valuable insights into canopy cover. Previous studies have shown the efficacy of using the complement of selected metrics in estimating AGB [50, 52, 53]. Our approach aligns with prior research that utilized the best subsets regression method, which was determined to be efficacious in identifying the optimal multiple linear regression (MLR) model [47, 52].

Model comparison

Model 1 (Eq. 3), in which we estimated the AGB using the relationship between field AGB estimates and UAS-lidar metrics, yielded the best results overall (Adj-R² = 0.84, rRMSE = 14.7%). It outperformed models 2 and 3, which predicted AGB using Sentinel-2 metrics. This is not surprising considering that lidar data, unlike optical images represents 3-dimensional vegetation structure [67, 68]. Model 1 also performed better than Mauya et al. [16], who estimated AGB using airborne-lidar in the Miombo woodlands of Tanzania (rRMSE 46.8%). Point cloud densities may have caused the variation in AGB estimate accuracy [16]. The airborne-lidar system utilized in Mauya et al. [16] had an average point density of 1.8 pts m⁻², whereas the UAS-lidar employed in this study had 300 pts m⁻². Since canopy height determination relies on the DTM, a greater point density will result in a better terrain surface model and more accurate canopy height determination [69–71]. Model 2 (Eq. 4) used the relationship between UAS-lidar estimated AGB from model 1 with Sentinel-2 image metrics to estimate the AGB for the entire study area, achieving (Adj-R² = 0.7, rRMSE

= 28.9%), which was obviously less precise than model 1, but achieved better results than model 3, which used direct relationship between field estimated AGB and Sentinel-2 metrics to estimate AGB. These findings confirm work by Wang et al. [32], who employed UAS-lidar and Sentinel-2 imagery to estimate AGB in mangrove forests, northeastern Hainan island, China. The better performance of model 2 can be attributed to the large number of UAS-lidar estimated AGB reference points as well as the sampling strategy (Fig. 2), which precisely linked the UAS-lidar data and Sentinel-2 data to a common location on the ground.

UAS-lidar as reference data

Previous research has shown that utilizing UAS imagery data to replace field data as reference data in a two-phase sampling approach is feasible [30, 32]. This was demonstrated in this study when UAS-lidar estimated AGB was used as reference data to estimate AGB using Sentinel-2 imagery for the entire study area, achieving ($\text{Adj-R}^2 = 0.70$), comparable to a study by Maurya et al. [16] who used airborne-lidar to estimate AGB in the Miombo woodlands of Tanzania and achieved ($\text{Adj-R}^2 = 0.69$). The positive relationship between UAS-lidar estimated AGB and Sentinel-2 image metrics exhibited in this study has benefits with synergistic potential to improve AGB estimation in the Miombo ecoregion. On the one hand, UAS-lidar offers the benefits of flexible deployment, affordability, and the capacity to capture precise vertical structure of vegetation, but it has drawbacks in terms of poor area coverage and massive processing and storage memory requirements [22, 72]. On the other hand, we have multi-spectral Sentinel-2 imagery, which is suitable for wall-to-wall coverage at 10 m resolution with NIR, red-edge, and SWIR bands, and a short revisit period of 5 days that it is useful for AGB estimation but falls short of capturing the fine vertical vegetation structure details that are required for forest management at a local level [2, 21]. The findings of this study validate UAS data's

capacity to deliver comprehensive training and validation information, which would have otherwise taken a significant amount of time and money utilizing field inventory processes. Furthermore, Sentinel-2-based AGB estimation offers a viable technique for broadening the scope of assessments beyond UAS-surveyed areas, boosting the efficiency of AGB estimation and monitoring operations. Previous research conducted on the estimation of AGB in the Miombo forests using direct ground to medium resolution Landsat data has shown suboptimal model fit. Kashindye et al. [14] found R^2 values ranging from 0.47 to 0.65 in their research conducted in Babati district, Tanzania. Their finding falls within a similar range as the study conducted by Halperin et al. [19] in Nyimba district, Zambia, where the R^2 ranged from 0.35 to 0.59 and it agrees with what was found utilizing direct ground to Sentinel-2 estimation in the present study ($\text{R}^2 = 0.62$). These were all lower than the estimations derived in this work by ground-UAS-Lidar-Sentinel-2 two-phase sampling ($\text{R}^2 = 0.79$). Hence, the integration of the two remote sensing data sources, as exemplified in this research, in conjunction with field techniques, enables the estimation of AGB in the Miombo woodlands with comprehensive accuracy that surpasses the individual capabilities of either data source, as evinced in prior studies [32, 73, 74].

Benefits of two phase-sampling

Estimation of AGB across vast Miombo woodlands is often restricted by the difficulty in obtaining sufficient field measurements owing to a variety of reasons such as limited labour, limited financial resources, remoteness, and poor access to their location. Most Miombo woodlands AGB estimation studies are undertaken over small regions or at a local scale using either destructive sampling [7, 8, 75] or remote sensing methods [13, 16] and a modest number of field samples. The two-phase sampling approach

has demonstrated how UAS-lidar could be used to upscale the field sampling to cover extensive areas, even with few field sample plots. From a mod-est 54 field points in phase 1, we were able to upscale to 700 UAS-lidar sample points in phase 2 to cover extensive areas and easily relate between UAS-lidar estimated AGB and Sentinel-2 metrics to estimate AGB over an expanded area covered by the Sentinel-2 image. The benefits of using the upscaling UAS-Lidar-Sentinel-2 imagery model ($\text{adj-R}^2 = 0.70$) as opposed to the direct field Plots-Sentinel-2 imagery model ($\text{adj-R}^2 = 0.55$) to estimate AGB have been demonstrated. The reason for an improved result from the UAS-lidar sampling technique could be because UAS-lidar covers a larger area with more points representing a wide range of vertical and horizontal vegetation structural changes and accurately measures terrain morphology. Then, using the UAS-lidar estimated AGB as training samples, the model can fit AGB variations over the entire study area and generate high prediction accuracy. This assertion is supported by earlier studies that employed lidar as a sampling tool for biomass estimation [25, 26, 32]. Though not investigated in this study, earlier studies have demonstrated that UAS-lidar sampling reduces the required number of field samples and the overall sampling cost [30, 32]. Previous research, however, has shown that optical Sentinel-2 images may become saturated in densely forested regions. This saturation problem may negatively impact AGB estimations. Nonetheless, Wang et al. [78] showed that adding Sentinel-1 synthetic aperture radar (SAR) data might assist reduce saturation and improve AGB estimates over wide regions. They did so by using data from UAS-Lidar, Sentinel-1, and Sentinel-2 satellites to estimate AGB for regional coniferous forests in China. Similarly, Navarro et al. [29] estimated AGB in Senegalese mangrove plantations using UAS-SfM point clouds, Sentinel-1, and Sentinel-2 data. The outcomes of this research and other related studies suggest that this technique can be used for improved AGB estimation for the entire Miombo ecoregion.

Arguably, the best approach could have been using most accurate UAS-lidar to estimate the AGB for estimating the AGB for the whole study area. But UAS-lidar has limitations in terms of area covered per flight, storage space and processing speed [22, 23], which makes it cumbersome to cover extensive areas. In the present study, for example, the coverage area achieved during each flight utilizing our UAS was limited to 30–40 hectares. Moreover, the point clouds from flight (one UAS-lidar block) required 30–40 Giga Bytes (GB) of storage space for processing. These factors provided a substantial challenge for our field laptop, which had just 150 GB of free space, restricting us to processing three blocks at a time and backing them up to an external drive before moving on to the next batch. With all of the aforementioned problems and what the literature has adequately stated [22, 23], it can be concluded that the utilization of UAS-lidar technology is currently limited to small sites and can only serve as a sampling tool for larger sites.

Conclusion

A two-phase sampling approach was used to estimate total AGB in the Miengwe forest reserve in the Miombo woodlands of Zambia. The findings of this study show the potential of using UAS-lidar as a sampling tool for estimating and monitoring AGB and other forest structural attributes across vast regions using wall-to-wall Sentinel-2 imagery when field data are limited. The AGB estimates are of a precision that is suitable for local forest management and international reporting mechanisms such as REDD + and MRV. The approach used in this study could be up-scaled to provide spatially consistent, low cost and precise AGB estimates over extensive regions for supporting the long-term sustainability of carbon monitoring and reporting initiatives in Miombo woodlands. The continuous improvement and reduction in cost of UAS-lidar technology and the continuous availability of wall-to-wall optical imagery such as Sentinel-2 assure viability

and warrant further investigation and refinement of this approach for future wall-to-wall carbon monitoring and reporting programs in the Miombo ecoregion.

Acknowledgements

This research was funded by The United States Agency for International Development through Partnerships for Enhanced Engagement in Research (PEER) program (Grant number 2000009945). Additional funding was provided by Oliver R Tambo African Research Chair Initiative (ORTARChI) project, an initiative of Canada's International Development Research Centre (IDRC), South Africa's National Research Foundation (NRF) and the Department of Science and Innovation (DSI), in partnership with the Oliver & Adelaide Tambo Foundation (OATF) and National Science and Technology Council, Zambia. The findings and conclusions in this publication are those of the authors and should not be construed to represent any official USDA or U.S. Government determination or policy.

Author contributions

HS: conceptualization, methodology, formal analysis, investigation, fieldwork, writing—original draft, writing—editing. SS: conceptualization, investigation, resources, writing—original draft, writing—review and editing, funding acquisition. PWC: Writing—review and editing. JCZ: writing—review and editing. AR: resources, writing—review and editing. ATH: investigation, writing—review and editing, funding acquisition. FH: fieldwork, writing—review and editing. All authors read and approved the final manuscript.

Funding

This study was funded by United States Agency for International Development through Partners for Enhanced Engagement in Research,

2000009945, Oliver R Tambo African Research Chair Initiative, 136557.

Data availability

The data that support the findings of this study are available from the corresponding author upon reasonable request.

Declarations

Ethics approval and consent to participate Not applicable.

Consent for publication

Not applicable.

Competing interests

The authors declare that they have no known competing financial interests or personal relationships that could have appeared to influence the work reported in this paper.

Received: 5 December 2023

Accepted: 17 May 2024

Published online: 08 June, 2024.

References

1. Barquín L, Chacón M, Panfil S, Adeleke A, Florian E, Triraganon R. The Knowledge and Skills Needed to Engage in REDD+: A Competencies Framework. Conservation International. Arlington, Virginia, USA. 2014.
2. Day M, Gumbo D, Moombe KB, Wijaya A, Sunderland T. Zambia country profile monitoring, reporting and verification for REDD +. Occas Pap. 2014. <https://doi.org/10.13140/2.1.2815.7121>.
3. Kerr JT, Ostrovsky M. From space to species: Ecological applications for remote sensing. *Trends Ecol Evol.* 2003;18:299–305.
4. Romijn E, Herold M, Kooistra L, Murdiyarso D, Verchot L. Assessing capacities of non-Annex I countries for national forest monitoring in the context of REDD +. *Environ Sci Policy.* 2012;19–20:33–48. <https://doi.org/10.1016/j.envsci.2012.01.005>.

5. Turner W, Spector S, Gardiner N, Fladeland M, Sterling E, Steininger M. Remote sensing for biodiversity science and conservation. *Trends Ecol Evol.* 2003;18:306–14.
6. White JC, Wulder MA, Varhola A, Vastaranta M, Coops NC, Cook BD, Pitt D, Woods M. A best practices guide for generating forest inventory attributes from airborne laser scanning data using an area-based approach. *For Chron.* 2013. <https://doi.org/10.5558/tfc2013-132>.
7. Handavu F, Syampungani S, Sileshi GW, Chirwa PWC. Aboveground and below-ground tree biomass and carbon stocks in the Miombo woodlands of the Copperbelt in Zambia. *Carbon Manag.* 2021;12:307–21. <https://doi.org/10.1080/17583004.2021.1926330>.
8. Kachamba DJ, Eid T, Gobakken T. Above- and belowground biomass models for trees in the Miombo woodlands of Malawi. *Forsts.* 2016. <https://doi.org/10.3390/f7020038>.
9. Mugasha W, Eid T, Bollandas OM, Malimbwi RE, Chamshama SA, Zahabu E, Katani JZ. Allometric models for prediction of aboveground biomass of single trees in Miombo woodlands in Tanzania. In: *Proceedings of the first Climate Change Impacts, Mitigation and Adaptation Programme Scientific Conference.* 2012. p. 8–17.
10. Hosonuma N, Herold M, De Sy V, De Fries RS, Brockhaus M, Verchot L, Angelsen A, Romijn E. An assessment of deforestation and forest degradation drivers in developing countries. *Environ Res Lett.* 2012;7:1–12.
11. Weisberg PJ, Dilts TE, Greenberg JA, Johnson KN, Pai H, Sladek C, Kratt C, Tyler SW, Ready A. Phenology-based classification of invasive annual grasses to the species level. *Remote Sens Environ.* 2021;263:112568. <https://doi.org/10.1016/j.rse.2021.112568>.
12. Halperin J, LeMay V, Chidumayo E, Verchot L, Marshall P. Model-based estimation of above-ground biomass in the Miombo ecoregion of Zambia. *For Ecosyst.* 2016. <https://doi.org/10.1186/s40663-016-0077-4>.
13. Kachamba DJ, Ørka HO, Gobakken T, Eid T, Mwase W. Biomass estimation using 3D data from unmanned aerial vehicle imagery in a tropical woodland. *Remote Sens.* 2016;8:968.
14. Kashindye A, Mtalo E, Mpanda MM, Liwa E, Giliba R. Multi-temporal assessment of forest cover, stocking parameters and above-ground tree biomass dynamics in Miombo Woodlands of Tanzania. *Afr J Environ Sci Technol.* 2013;7:611–23.
15. Mareya HT, Tagwireyi P, Ndaimani H, Gara TW, Gwenzi D. Estimating tree crown area and aboveground biomass in Miombo woodlands from high-resolution RGB-only imagery. *IEEE J Sel Top Appl Earth Obs Remote Sens.* 2018;11:868–75.
16. Mauya EW, Ene LT, Bollandas OM, Gobakken T, Næsset E, Malimbwi RE, Zahabu E. Modelling aboveground forest biomass using airborne laser scanner data in the Miombo woodlands of Tanzania. *Carbon Balance Manag.* 2015;10:1–16.
17. Næsset E, Ørka HO, Solberg S, Bollandas OM, Hansen EH, Mauya E, Zahabu E, Malimbwi R, Chamuya N, Olsson H, Gobakken T. Mapping and estimating forest area and aboveground biomass in Miombo woodlands in Tanzania using data from airborne laser scanning, TanDEM-X, RapidEye, and global forest maps: a comparison of estimated precision. *Remote Sens Environ.* 2016;175:282–300. <https://doi.org/10.1016/j.rse.2016.01.006>.
18. Samimi C, Kraus T. Biomass estimation using Landsat-TM and -ETM+: towards a regional model for Southern Africa? *GeoJournal.* 2004;59:177–87.
19. Halperin J, LeMay V, Coops N, Verchot L, Marshall P, Lochhead K. Remote sensing of environment canopy cover estimation in Miombo woodlands of Zambia: comparison of Landsat 8 OLI versus RapidEye imagery using parametric, nonparametric, and semiparametric methods. *Remote Sens Environ.* 2016;179:170–82. <https://doi.org/10.1016/j.rse.2016.03.028>.
20. Xie Y, Sha Z, Yu M. Remote sensing imagery in vegetation mapping: a review. *J Plant Ecol.* 2008;1:9–23.
21. Goetz SJ, Hansen M, Houghton RA, Walker W, Laporte N, Busch J. Measurement and monitoring needs, capabilities and potential for addressing reduced emissions from deforestation and forest degradation under. *Environ Res Lett.* 2015;10:123001.
22. Shamaoma H, Chirwa PW, Ramoelo A, Hudak AT, Syampungani S. The application of UASs in forest management and monitoring: challenges and opportunities for use in the Miombo woodland. *Forsts.* 2022;13:1812.
23. Whitehead K, Hugenholtz CH, Myshak S, Brown O, Leclair A, Tamminga A, Barchyn TE, Moorman B, Eaton B. Remote sensing of the environment with small unmanned aircraft systems (UASs), part 2: scientific and commercial applications 1. *J Unmanned Veh Syst.* 2014;102:86–102.
24. Korhonen L, Morsdorf F. Estimation of canopy cover, gap fraction and leaf area index with airborne laser. In: Maltamo M, Næsset E, Vauhkonen J, editors. *Forest applications of airborne laser scanning: concepts and case studies.* Dordrecht: Springer; 2014. p. 397–417.
25. Matasci G, Hermosilla T, Wulder MA, White JC, Coops NC, Hobart GW, Zald HSJ. Large-area mapping of Canadian boreal forest cover, height, biomass and other structural attributes using Landsat composites and lidar plots. *Remote Sens Environ.* 2018;209:90–106. <https://doi.org/10.1016/j.rse.2017.12.020>.
26. Nelson R, Margolis H, Montesano P, Sun G, Cook B, Corp L, Andersen HE, deJong B, Pellat FP, Fickel T, Kauffman J, Prisley S. Lidar-based estimates of aboveground biomass in the continental US and Mexico using ground, airborne, and satellite observations. *Remote Sens Environ.* 2017;188:127–40. <https://doi.org/10.1016/j.rse.2016.10.038>.
27. Su Y, Guo Q, Xue B, Hu T, Alvarez O, Tao S, Fang J. Spatial distribution of forest aboveground biomass in China: estimation through combination of spaceborne lidar, optical imagery, and forest inventory data. *Remote Sens Environ.* 2016;173:187–99. <https://doi.org/10.1016/j.rse.2015.12.002>.
28. Wang D, Wan B, Qiu P, Zuo Z, Wang R, Wu X. Mapping height and above-ground biomass of mangrove forests on Hainan Island using UAV-LiDAR sampling. *Remote Sens.* 2019;11:1–25.
29. Navarro JA, Algeet N, Fernández-Landa A, Esteban J, Rodríguez-Noriega P, Guillén-Climent ML. Integration of UAV, Sentinel-1, and Sentinel-2 data for mangrove plantation aboveground biomass monitoring in Senegal. *Remote Sens.* 2019;11:1–23.
30. Puliti S, Ene LT, Gobakken T, Næsset E. Use of partial-coverage UAV data in sampling for large scale forest inventories. *Remote Sens Environ.* 2017;194:115–26. <https://doi.org/10.1016/j.rse.2017.03.019>.
31. Wulder MA, White JC, Nelson RF, Næsset E, Ørka HO, Coops NC, Hilker T, Bater CW, Gobakken T. Lidar sampling for large-area forest characterization: a review. *Remote Sens Environ.* 2012;121:196–209. <https://doi.org/10.1016/j.rse.2012.02.001>.
32. Wang D, Wan B, Liu J, Su Y, Guo Q, Qiu P, Wu X. Estimating aboveground biomass of the mangrove forests on northeast Hainan Island in China using an upscaling method from field plots, UAV-LiDAR data and Sentinel-2 imagery. *Int J Appl Earth Obs Geoinf.* 2020;85:101986. <https://doi.org/10.1016/j.jag.2019.101986>.
33. Mlambo R, Woodhouse IH, Gerard F, Anderson K. Structure from motion (SfM) photogrammetry with drone data: a low cost structure from motion (SfM) photogrammetry with drone data: a low cost method for monitoring greenhouse gas emissions from forests in developing countries. *Forsts.* 2017;8:68.
34. Nelson R, Boudreau J, Gregoire TG, Margolis H, Næsset E, Gobakken T, Ståhl G. Estimating Quebec provincial forest resources using ICESat/GLAS. *Can J For Res.* 2009;39:862–81.
35. Zhao X, Guo Q, Su Y, Xue B. Improved progressive TIN densification filtering algorithm for airborne LiDAR data in forested areas. *ISPRS J Photogramm Remote Sens.* 2016;117:79–91. <https://doi.org/10.1016/j.isprs.jprs.2016.03.016>.
36. ESA. 2022. European Space Agency. Sentinel. <https://sentinel.esa.int/web/sentinel/user-guides/sentinel-1-sar/acquisition-modes/interferometric-wide-swath>. Accessed 6 Dec 2022.
37. ESRI. ArcGIS Desktop: release 10.7.1. Redlands: Environmental Systems Research Institute; 2019.
38. Mauya EW, Madundo S. Modelling above ground biomass using Sentinel 2 and planet

- scope data in dense tropical montane forests of Tanzania. *Tanzania J For Nat Conserv*. 2022;91:132–53.
39. Muhe S, Argaw M. Estimation of above-ground biomass in tropical afro-montane forest using Sentinel-2 derived indices. *Environ Syst Res*. 2022. <https://doi.org/10.1186/s40068-022-00250-y>.
40. Bullock EL, Woodcock CE, Olofsson P. Remote sensing of environment monitoring tropical forest degradation using spectral unmixing and Landsat time series analysis. *Remote Sens Environ*. 2018. <https://doi.org/10.1016/j.rse.2018.11.011>.
41. Souza CM, Roberts DA, Cochrane MA. Combining spectral and spatial information to map canopy damage from selective logging and forest fires. *Remote Sens Environ*. 2005;98:329–43.
42. Souza CM, Siqueira JV, Sales MH, Fonseca AV, Ribeiro JG, Numata I, Cochrane MA, Barber CP, Roberts DA, Barlow J. Ten-year Landsat classification of deforestation and forest degradation in the Brazilian Amazon. *Remote Sens*. 2013;5:5493–513.
43. Shi C, Wang L. Incorporating spatial information in spectral unmixing: a review. *Remote Sens Environ*. 2014;149:70–87. <https://doi.org/10.1016/j.rse.2014.03.034>.
44. SEPAL. System for earth observation data access, processing and analysis for land monitoring. <https://sepal.io>. Accessed 13 Apr 2023.
45. Fassnacht FE, Hartig F, Latifi H, Berger C, Hernández J, Corvalán P, Koch B. Importance of sample size, data type and prediction method for remote sensing-based estimations of aboveground forest biomass. *Remote Sens Environ*. 2014;154:102–14.
46. Minitab L. Minitab. 2023. <https://www.minitab.com>. Accessed 23 Jan 2023.
47. Hudak AT, Crookston NL, Evans JS, Falkowski MJ, Smith AMS, Gessler PE, Morgan P. Regression modeling and mapping of coniferous forest basal area and tree density from discrete-return lidar and multispectral satellite data. *Can J Remote Sens*. 2006;32:126–38.
48. Sugiura N. Further analysis of the data by Anaike's information criterion and the finite corrections. *Commun Stat Theory Methods*. 1978;7:13–26.
49. Brewer MJ, Butler A, Cooksley SL. The relative performance of AIC, AICC and BIC in the presence of unobserved heterogeneity. *Methods Ecol Evol*. 2016;7:679–92.
50. Liu K, Shen X, Cao L, Wang G, Cao F. Estimating forest structural attributes using UAV-LiDAR data in Ginkgo plantations. *ISPRS J Photogramm Remote Sens*. 2018;146:465–82. <https://doi.org/10.1016/j.isprsjprs.2018.11.001>.
51. Lu J, Wang H, Qin S, Cao L, Pu R, Li G, Sun J. Estimation of aboveground biomass of Robinia pseudoacacia forest in the Yellow River Delta based on UAV and Backpack LiDAR point clouds. *Int J Appl Earth Obs Geoinf*. 2020;86:102014.
52. Cao L, Liu H, Fu X, Zhang Z, Shen X, Ruan H. Comparison of UAV LiDAR and digital aerial photogrammetry point clouds for estimating forest structural attributes in subtropical planted forests. *Forests*. 2019;1–26. <https://doi.org/10.3390/f10020145>.
53. Bouvier M, Durrieu S, Fournier RA, Renaud JP. Generalizing predictive models of forest inventory attributes using an area-based approach with airborne LiDAR data. *Remote Sens Environ*. 2015;156:322–34. <https://doi.org/10.1016/j.rse.2014.10.004>.
54. Li Y, Andersen H-E, McGaughey R. A Comparison of statistical methods for estimating data. *West J Appl For*. 2008;23:223–31.
55. Cao L, Coops NC, Hermosilla T, Innes J, Dai J, She G. Using small-footprint discrete and fullwaveform airborne LiDAR metrics to estimate total biomass and biomass components in subtropical forests. *Remote Sens*. 2014;6:7110–35.
56. Cao L, Liu K, Shen X, Wu X, Liu H. Estimation of forest structural parameters using UAV-LiDAR data and a process-based model in Ginkgo planted forests. *IEEE J Sel Top Appl Earth Obs Remote Sens*. 2019;12:4175–90.
57. Dube T, Mutanga O, Cletah S, Adelabu S, Tsitsi B. Remote sensing of aboveground forest biomass: A review. *Trop Ecol*. 2016;57:125–32.
58. Hopkinson C. The influence of flying altitude, beam divergence, and pulse repetition frequency on laser pulse return intensity and canopy frequency distribution. *Can J Remote Sens*. 2007;33:312–24.
59. Næsset E. Effects of different sensors, flying altitudes, and pulse repetition frequencies on forest canopy metrics and biophysical stand properties derived from small-footprint airborne laser data. *Remote Sens Environ*. 2009;113:148–59. <https://doi.org/10.1016/j.rse.2008.09.001>.
60. Miller JD, Thode AE. Quantifying burn severity in a heterogeneous landscape with a relative version of the delta Normalized Burn Ratio (dNBR). *Remote Sens Environ*. 2007;109:66–80.
61. Wallis CIB, Homeier J, Peña J, Brandl R, Farwig N, Bendix J. Modeling tropical montane forest biomass, productivity and canopy traits with multispectral remote sensing data. *Remote Sens Environ*. 2019;225:77–92. <https://doi.org/10.1016/j.rse.2019.02.021>.
62. Adam E, Mutanga O, Abdel-Rahman EM, Ismail R. Estimating standing biomass in papyrus (*Cyperus papyrus* L.) swamp: exploratory of in situ hyperspectral indices and random forest regression. *Int J Remote Sens*. 2014;35:693–714. <https://doi.org/10.1080/01431161.2013.870676>.
63. Dang ATN, Nandy S, Srinet R, Luong NV, Ghosh S, Senthil Kumar A. Forest aboveground biomass estimation using machine learning regression algorithm in Yok Don National Park, Vietnam. *Ecol Inform*. 2019;50:24–32. <https://doi.org/10.1016/j.ecoinf.2018.12.010>.
64. Moradi F, Sadeghi SMM, Heidarlou HB, Deljouei A, Boshkar E, Borz SA. Above-ground biomass estimation in a Mediterranean sparse coppice oak forest using Sentinel-2 data. *Ann For Res*. 2022;65:165–82.
65. Castillo JAA, Apan AA, Maraseni TN, Salmo SG. Estimation and mapping of above-ground biomass of mangrove forests and their replacement land uses in the Philippines using Sentinel imagery. *ISPRS J Photogramm Remote Sens*. 2017;134:70–85. <https://doi.org/10.1016/j.isprsjprs.2017.10.016>.
66. White JC, Wulder MA, Vastaranta M, Coops NC, Pitt D, Woods M. The utility of image-based point clouds for forest inventory: a comparison with airborne laser scanning. *Forests*. 2013;4:518–36.
67. Lim K, Treitz P, Wulder M, Flood M. LiDAR remote sensing of forest structure. *Prog Phys Geogr*. 2003;27:88–106.
68. Maltamo M, Naesset E, Vauhkonen J. Forestry applications of airborne laser scanning. Dordrecht: Springer; 2014.
69. Cunliffe AM, Assmann JJ, Daskalova GN, Kerby JT, Myers-Smith IH. Above-ground biomass corresponds strongly with drone-derived canopy height but weakly with greenness (NDVI) in a shrub tundra landscape. *Environ Res Lett*. 2020;15:125004.
70. Kato A, Moskal LM, Schiess P, Swanson ME, Calhoun D, Stuetzle W. Capturing tree crown formation through implicit surface reconstruction using airborne lidar data. *Remote Sens Environ*. 2009;113:1148–62. <https://doi.org/10.1016/j.rse.2009.02.010>.
71. Nandy S, Srinet R, Padalia H. Mapping forest height and aboveground biomass by integrating ICESat-2, Sentinel-1 and Sentinel-2 data using Random Forest algorithm in northwest Himalayan foothills of India. *Geophys Res Lett*. 2021;48:1–10.
72. Guo Q, Su Y, Hu T, Zhao X, Wu F, Li Y, Liu J, Chen L, Xu G, Lin G, Zheng Y, Lin Y, Mi X, Fei L, Wang X. An integrated UAV-borne lidar system for 3D habitat mapping in three forest ecosystems across China. *Int J Remote Sens*. 2017. <https://doi.org/10.1080/01431161.2017.1285083>.
73. Mao P, Ding J, Jiang B, Qin L, Qiu GY. How can UAV bridge the gap between ground and satellite observations for quantifying the biomass of desert shrub community? *ISPRS J Photogramm Remote Sens*. 2022;192:361–76. <https://doi.org/10.1016/j.isprsjprs.2022.08.021>.
74. Riikimäki H, Luoto M, Heiskanen J. Estimating fractional cover of tundra vegetation at multiple scales using unmanned aerial systems and optical satellite data. *Remote Sens Environ*. 2019;224:119–32. <https://doi.org/10.1016/j.rse.2019.01.030>.
75. Mugasha WA, Eid T, Bollandsås OM, Malimbwi RE, Chamshama SAO, Zahabu E, Katani JZ. Allometric models for predic-

tion of above- and belowground biomass of trees in the Miombo woodlands of Tanzania. For Ecol Manag. 2013;310:87–101. <https://doi.org/10.1016/j.foreco.2013.08.003>.


76. Xue J, Su B. Significant remote sensing vegetation indices: a review of developments and applications. J Sens. 2017;2017:1–17.
77. Askar, Nuthammachot N, Phairuang W, Wicaksono P, Sayektiningsih T. Estimating aboveground biomass on private forest using sentinel-2 imagery. J Sens. 2018. <https://doi.org/10.1155/2018/6745629>.
78. Wang Y, Jia X, Chai G, Lei L, Zhang X. Improved estimation of above-ground biomass of regional coniferous forests integrating UAV-LiDAR strip data, Sentinel-1 and Sentinel-2 imageries. Plant Methods. 2023;19:1–19. <https://doi.org/10.1186/s13007-023-01043-9>.

Publisher's Note

Springer Nature remains neutral with regard to jurisdictional claims in published maps and institutional affiliations.

The paper is originally published in Plant Methods (2024) 20:88 <https://doi.org/10.1186/s13007-024-01212-4>.

Open Access This article is licensed under a Creative Commons Attribution 4.0 International License, which permits use, sharing, adaptation, distribution and reproduction in any medium or format, as long as you give appropriate credit to the original author(s) and the source, provide a link to the Creative Commons licence, and indicate if changes were made. The images or other third party material in this article are included in the article's Creative Commons licence, unless indicated otherwise in a credit line to the material. If material is not included in the article's Creative Commons licence and your intended use is not permitted by statutory regulation or exceeds the permitted use, you will need to obtain permission directly from the copyright holder. To view a copy of this licence, visit <http://creativecommons.org/licenses/by/4.0/>. The Creative Commons Public Domain Dedication waiver (<http://creativecommons.org/publicdomain/zero/1.0/>) applies to the data made available in this article, unless otherwise stated in a credit line to the data.

The paper is republished with authors' permission. 

e-GEOS and Umbra partnership

e-GEOS and Umbra have signed a multi-year strategic agreement to jointly develop innovative geospatial intelligence solutions for customers worldwide.

The deal will combine the high revisit frequency, resolution and wide coverage offered by the First and Second Generation COSMO-SkyMed satellites – a SAR program of the Italian Space Agency and the Italian Ministry of Defense for which e-GEOS is the exclusive licensee of data for commercial users – with Umbra's agile SAR constellation and imagery. e-GEOS will apply its proprietary artificial intelligence solutions to Umbra's SAR data to develop and introduce new analytics products to the market. www.e-geos.it

Norway poised to lead in 3D city modelling

Detailed map data could soon bring Norwegian cities to life in three dimensions. A new pilot project suggests that it is exceptionally well placed to create realistic digital city models, thanks to its high-quality 2.5D vector data. The findings are presented in the newly released report called 'Preliminary Project – Volume Geometry in Norwegian Geodata Management', now available on the Norwegian Mapping Authority's website.

The study explored how municipalities currently use 3D representations – known as volume geometry – in urban planning and building management, as well as the challenges they face in data quality and integration. Conducted between October 2024 and June 2025, the project was funded by Geovekstforum and the Research Council of Norway.

The working group concludes that volume geometry should continue to be treated as a derived product, created from 2.5D vector data and other sources, rather than as a standalone dataset. To improve accuracy, a dedicated test project is recommended, focusing on more detailed data and enhanced quality control. Based on the outcomes of

such a test, the FKB dataset (Norway's national large-scale mapping database) could then be further developed to better support three-dimensional modelling.


CityGML, the internationally recognized standard for 3D city models, is identified as the most suitable format for Norwegian volume datasets, though the group stresses the need for a clear national specification to guide its implementation. Furthermore, the costs and benefits of establishing a public dataset should be assessed as a possible alternative to commercial solutions. Finally, the group recommends strengthening object-based management to ensure greater coherence between different data representations and uses.

IIT Bhubaneswar and Survey of India partnership

Indian Institute of Technology (IIT) Bhubaneswar and the Odisha & Chhattisgarh Geo-Spatial Directorate of the Survey of India (SoI) signed a MoU on 25 November 2025 to strengthen collaboration in the areas of Geodesy, Geo-informatics, mapping technologies, and geospatial research. Both institutions will work together to facilitate the exchange of scientific and technical information, enhance research capabilities, and drive innovation in emerging geospatial technologies. www.iitbbs.ac.in

Delivering advanced hazard intelligence

ICEYE announced a new partnership with Boustead Geospatial and Esri Australia, to bring ICEYE's suite of near real-time hazard insights to customers across Australia. The collaboration, facilitated through the Boustead Geospatial Group, will deliver ICEYE's Flood Rapid Intelligence, Flood Insights, and Bushfire Insights as ready-to-use map layers within the ArcGIS platform.

For organisations already using Esri's GIS technology, ICEYE's data will now be available directly through ArcGIS Online. www.iceye.com 

UAVOS partners to advance HAPS technology

UAVOS has announced the successful completion of a test flight of Mira Aerospace's High-Altitude Pseudo-Satellite (HAPS) ApusNeo 18, with UAVOS providing full engineering and technical support. One of the key objectives of the flight was to evaluate the jointly developed optoelectronic, gyro-stabilized aircraft POD (Payload Onboard Device) by obtaining imagery from altitudes ranging between 3,000 and 12,000 meters. During the mission, the POD captured high-resolution imagery with precise geolocation data from an altitude of 12,000 meters, achieving a Ground Sample Distance (GSD) of up to two meters. The test took place in Abu Dhabi, UAE, and lasted continuously for 48 hours.

The optoelectronic gyro-stabilized aircraft POD is equipped with an innovative automatic temperature control system for heating and cooling electronic modules, ensuring reliable operation in the stratosphere at temperatures as low as -70°C under rarefied air conditions. The system also provides radio communication at distances exceeding 100 km. The gimbal's optical unit allows observation within a $\pm 90^\circ$ range with high-precision angular positioning. The payload housing features an aerodynamically optimized design, and the total payload weight is 3.6 kg. www.uavos.com

ideaForge and C-DAC sign strategic MoU

ideaForge Technology Limited, Indian UAS manufacturer has signed a strategic MoU with the Centre for Development of Advanced Computing (C-DAC) to strengthen drone-led emergency response across India and jointly advance research in next-generation UAV, semiconductor and data-driven technologies.

The partnership brings together ideaForge's FLYGHT platform, a ready-to-deploy, on-demand drone network delivered through a Drone-as-a-Service (DaaS) model, with C-DAC's Emergency

Response Support System (ERSS-Dial 112), which enables anyone to access emergency services such as police, fire or medical assistance through a single nationwide emergency number. With India's average emergency response time nearing twenty minutes, integrating FLYGHT into ERSS will significantly improve response efficiency by enabling drones to serve as rapid first responders. www.ideaforgetech.com

Indrajaal unveils India's first anti drone patrol vehicle

Indrajaal Drone Defence has announced the launch of India's first Anti-Drone Patrol Vehicle (ADPV) — fully mobile, AI-enabled counter-drone system. The urgency to build the ADPV (Indrajaal Ranger) was reinforced by two recent national security incidents that exposed how drones have become a critical link in breaching India's border security.

First, the ISI-linked cross-border drone-trafficking incident — where weapons were smuggled deep into Indian territory — exposed a stark reality: illegal border drone movement today is as good as welcoming weapons into our cities. Second, the BSF neutralising 255 Pakistani drones so far this year underscored how drones have become the primary transport channel for India's ₹3-lakh-crore drug-trafficking ecosystem. indrajaal.in

MatrixSpace launches portable 360Radar

Portable 360 Radar by MatrixSpace is a rugged, easily transportable radar kit delivers reliable close-airspace awareness with panoramic coverage for rapid-response counter-drone operations, from safe-guarding stadiums and large public gatherings, to border security and battlespaces. It unifies threat awareness across multiple networked Portable 360 Radar systems and other sensors, without compromising local operation. By combining AI edge processing with MatrixSpace AiCloud Enterprise Software, central/remote command centers get an enhanced common operating picture and

deep airspace activity analytics to assure public safety. www.matrixspace.com

AeroVironment expands Puma™ VNS kit

AeroVironment, Inc. recently announced the integration of its Visual Navigation System (VNS) kit with the Puma™ Long Endurance (LE) small unmanned aircraft system (SUAS), delivering GNSS-denied navigation capability to ensure mission success.

It uses advanced computer vision and onboard processing to deliver precise, GNSS-independent navigation, and its integration into Puma LE now extends this capability across the full Puma family for greater flexibility and resilience in degraded or denied environments.

Using a suite of downward-facing sensors, cameras and onboard computing, the VNS kit performs Visual Inertial Odometry (VIO) to capture and analyze terrain imagery, estimating true aircraft position in real time. The system fuses continuous visual data from the cameras with motion inputs from onboard inertial sensors to calculate precise position, velocity, and orientation - allowing the aircraft to know where it is and where it is going when GNSS is not available. www.avinc.com

China launches new remote sensing satellite

China launched a Long March 4B carrier rocket on 9th December to place a new RS satellite, Yaogan 47, into space. The launch was the 614th flight mission of the Long March carrier rocket series.

China launches satellites for UAE, Egypt and Nepal

China launched the Kinetica-1, also known as the Lijian-1 Y11 carrier rocket with nine satellites onboard, including three international payloads for the United Arab Emirates (UAE), Egypt and Nepal. After delivering the nine satellites to their preset orbits, the launch mission was declared a complete success.

According to the rocket developer CAS Space, most of the satellites is owned by the Chinese Academy of Sciences (CAS). The Arab satellite 813 was developed by the Shanghai-based Innovation Academy for Microsatellites of CAS. It is a hyperspectral Earth observation satellite. It carries primary payloads including a hyperspectral imager, a panchromatic camera, and an atmospheric polarization corrector, along with the construction of corresponding ground systems.

The core aim of the project is to build hyperspectral remote sensing capabilities, thereby providing effective support for environmental monitoring and scientific research, according to the CAS Space. The name 813 honors the year that marked the rise of the House of Wisdom in Baghdad - an era of scientific flourishing that the project seeks to revive. www.globaltimes.cn

Foresight report 2030

The Association for Geographic Information has published its third foresight report, providing a visionary view of trends and influences over the next five years and beyond. Developed over 12 months, it explores six transformative forces shaping the geospatial sector: the Data Imperative, AI Integration Challenge, Infrastructure Evolution, Collaboration Imperative, Earth Systems.

The importance of open data has reached or exceeded expectations, while innovative technologies such as AI and data analytics have far exceeded expectations... driven, the authors say, largely by the needs presented by the COVID-19 pandemic. Conversely, the uptake and progress of BIM has “not progressed as rapidly as anticipated,” nor have ‘future cities’ ambitions born as much fruit as hoped. In addition, the previous report completely failed — understandably — to anticipate the generative AI revolution. www.agi.org

Moldova's positioning system now uses Galileo

The MOLDPOS National Positioning System in Moldova has been integrated into the European Position Determination System (EUPOS), a pan-European GNSS augmentation service. The MOLDPOS navigational system uses both GPS and GLONASS, and now Galileo has been added. Creation of MOLDPOS was gradual. First, sites for placement of MOLDPOS stations were selected, then the stations were installed. Once installations were in place, the system was tested and launched. Now it is integrated into EUPOS. Moldova had been a member of the European Position Determination System since 2008. moldpos.md

VIAVI wins U.S. DOT award to advance CPNT

Viavi Solutions Inc. has received an award from the U.S. Department of Transportation (DOT) through its Complementary Positioning, Navigation, and Timing (CPNT) Action Plan Rapid Phase II. It will integrate and test its SecureTimeSM altGNSS GEO-L service and SecurePNT™ 6200 resilient timing solution at the VIAVI Automated Lab-as-a-Service for Open RAN (VALOR™) and the Open RAN Center for Integration and Deployment (ORCID) labs. VALOR and ORCID are funded by the National Telecommunications and Information Administration (NTIA) Public Wireless Supply Chain Innovation Fund (PWSCIF). www.viavisolutions.com

SatLab launches SL8 laser RTK receiver

The SatLab SL8 Laser RTK Receiver integrates dual cameras, GNSS, IMU, and visible laser technology to simplify and accelerate surveying tasks. It provides non-contact measurement, image-assisted targeting, CAD live-view stakeout, and a built-in LoRa radio for reliable operation in complex or GNSS-limited environments. The Laser RTK achieves 2 cm accuracy within 10 meters and enables efficient data collection across

bridges, tunnels, riverbanks, and other sites where traditional GNSS methods are restricted. www.satlabgeo.com

Unjammable military communication by Astrolight

Lithuanian space and defense tech company Astrolight has successfully demonstrated undetectable and unjammable laser-based communication and data transmission with its POLARIS terminal during NATO's latest exercise. It placed two POLARIS laser terminals on land, operating continuously throughout all 9 days of the exercise, including in rain and fog. During the tests, POLARIS successfully demonstrated interoperability with military communication infrastructure, connecting a military base to an ad-hoc remote command post. astrolightspace.com

Galileo adds two new satellites

Europe has given fresh momentum to its Galileo navigation system following the successful launch on December 17 of two new satellites aboard an Ariane 6 rocket. This launch, the fourteenth of the program (L14), is one of the final three planned launches of first-generation (G1G) satellites. The new satellites will strengthen the global positioning, navigation, and timing services provided by the system.

The launch comes at a critical moment for the constellation, which faces the need to replace some of its oldest satellites. With millions of users worldwide routinely relying on Galileo services, this milestone ensures Europe's ability to operate its own radionavigation system. This launch paves the way for the L15 and L16 missions, which will complete the first generation of the system before transitioning to the second-generation Galileo satellites (G2G), currently under development. These will introduce advanced capabilities, greater accuracy, and enhanced resilience against interference and cyber threats, further strengthening Galileo's role as a strategic infrastructure for Europe. gmv.com

SiTime takes on GNSS threats

SiTime Corporation has launched the Endura® temperature compensated oscillator (Super-TCXO®), ENDR-TTT, for PNT applications. When GNSS signals are dropped due to unavailability or degradation - including signal jamming or extreme environmental conditions - holdover maintains timing stability locally to enable uninterrupted network operation. The ENDR-TTT Endura Super-TCXO provides up to 20x longer holdover and 20x better PNT accuracy, dramatically improving spoofing resistance. sitime.com

Second-gen spaceborne GNSS receiver by SpacePNT

SpacePNT has completed the extensive qualification testing of its second generation product, including vibrations, shocks, thermal vacuum and EMC. This second generation multi-frequency multi-GNSS receiver product is the result of two important ESA ARTES Competitive & Growth (C&G) development projects that have received support from the European Space Agency (ESA) and the Swiss Space Office (SSO).

The first ARTES C&G project has allowed SpacePNT to develop an industrialized second generation product suitable to be produced in larger quantities, i.e., targeting LEO/LEO-PNT/GEO telecom constellations, and embedding amongst other options a proprietary Precise Orbit Determination (POD) algorithm capable to provide sub-decimetre (3D rms) real-time positioning and timing onboard the spacecraft. Within the second ARTES C&G project, SpacePNT has developed a specific Radiation Hardness Assurance (RHA) approach that can be proposed as an option for very long duration missions operating in harsh radiation environments. spacepnt.com

Sinclair Technologies launches 5G GNSS antennas

Sinclair Technologies has launched its SM 5G Family Tier, featuring the SM714 and SM2601 series antennas. The next-generation, multi-band, multi-port transport antennas are engineered to

deliver superior connectivity, reliability and versatility for GNSS, 5G, LTE, Wi-Fi and other mission-critical wireless applications. www.sinctech.com

Topcon's autonomous steering package for farmers

Topcon's has created a Value Line Steering solution for farmers using mid-range tractors on small- to medium-sized farms. It makes autosteering technology - typically used on larger machinery - accessible to a broader range of farmers. The integrated system is designed to work across a wide range of applications, machinery and brands. It includes compliance with ISOBUS-UT to offer universal compatibility and ease of use. topconpositioning.com

Aurora Navigation unveils mobile visual RTK system

Aurora Navigation has launched the Astra1 Mobile Visual RTK, a professional-grade GNSS receiver engineered to redefine high-precision mobile data acquisition. www.auroranav.com

U-blox releases SIG 2.00 GNSS firmware

U-blox has released Standard Infrastructure GNSS (SIG) 2.00, a dedicated GNSS firmware solution for Wi-Fi 6E/7/8 access points operating in the 6 GHz band.

Designed to meet Automated Frequency Coordination (AFC) requirements in the U.S. and Canada, SIG 2.00 enables access points to determine their geolocation with 95% confidence-bound accuracy. It also delivers improved positioning accuracy under multipath environments, ensuring AFC systems receive reliable geolocation data. www.u-blox.com

infiniDome launches GNSS anti-jamming technology

infiniDome has introduced Aura, a new GNSS protection system built for platforms that cannot afford to lose

their way. The system is available in two configurations: Aura, the enclosed version for rapid deployment, and AuraCore, the OEM module for integration. The system brings mission-grade protection to platforms ranging from small UAVs to large autonomous vehicles. www.infinidome.com

Honeywell cleared for U.S. M-code military navigation

Honeywell has received U.S. government authorization for the remaining variants of its M-code GPS Inertial Navigation System (EGI). It was awarded the MSO-c145b authorization by the Precise Position Equipment Certification Office (PECO) for its smaller form factor embedded GPS EGI, known as the FALCN. With this new qualification, all of Honeywell's EGI offerings are certified and approved by the U.S. government. aerospace.honeywell.com

KONGSBERG taps Advanced Navigation in multi-million deal

Advanced Navigation has finalized a multi-million deal with Kongsberg Defence & Aerospace ('KONGSBERG'). Under the deal, Advanced Navigation will supply more than 50 Boreas D90 fiber-optic gyroscope inertial navigation systems (FOG INS) to strengthen KONGSBERG's PROTECTOR RS4 in high-threat, contested environments. www.advancednavigation.com

SPH Engineering launches high-resolution UAV GPR antennas

SPH Engineering is offering two new ground-penetrating radar systems optimized for UAV integration: MALÅ GeoDrone 600 and Zond Aero 600 NG.

Both 600 MHz antennas significantly enhance high-resolution subsurface investigations with drones. They enable surveyors to capture consistent, high-quality subsurface data in areas difficult, slow, or unsafe to access with traditional ground instruments. www.sphengineering.com

SUBSCRIPTION FORM

YES! I want my **Coordinates**

I would like to subscribe for (tick one)

☐ 1 year ☐ 2 years

12 issues

24 issues

Rs.2400/US\$200

Rs.4500/US\$350

Postage and handling charges extra.

First name

Last name

Designation

Organization

Address

.....

City Pincode

State Country

Phone

Fax

Email

I enclose cheque no.

drawn on

date towards subscription

charges for Coordinates magazine

in favour of 'Coordinates Media Pvt. Ltd.'

Sign Date

Mail this form with payment to:

Coordinates

A 002, Mansara Apartments

C 9, Vasundhara Enclave

Delhi 110 096, India.

If you'd like an invoice before sending your payment, you may either send us this completed subscription form or send us a request for an invoice at iwant@mycoordinates.org

MARK YOUR CALENDAR

February 2026

Geo Week

16 - 18, February 2026
Denver, CO, USA
www.geo-week.com

DGI 2026

23 -25 February
The Queen Elizabeth II Centre, London
<https://dgi.wbresearch.com>

March 2026

Munich Navigation Satellite Summit

25 - 27 March 2026
Munich, Germany
www.munich-satellite-navigation-summit.org

Geo Connect Asia, Digital Construction Asia,
Ocean Connect Asia, Drones & Uncrewed Asia
31st March - 01st April
Singapore
www.geoconnectasia.com

April 2026

Assured PNT Summit

7 - 8 April 2026
Washington DC, USA
<https://pnt.dsigroup.org>

4th Geospatial & Space Technology MENA Forum

8 - 9 April 2026
Dubai, United Arab Emirates
<https://menageospatialforum.com>

Pacific PNT conference

13 - 16, April 2026
Honolulu, Hawaii
<https://www.ion.org>

2026 Commercial UAV Forum

22 - 23 April
Amsterdam, The Netherlands
www.forumuav.com

European Navigation Conference 2026

28 - 30 April 2026
Vienna, Austria
<https://enc-series.org>

May 2026

Geolignite 2026

11 - 13, May
Ottawa, Canada
<https://geolignite.ca>

GISTAM 2026

21 - 23 May
Benidorm, Spain
<https://gistam.scitevents.org>

FIG 2026

24 - 29 May
Cape Town, South Africa
<https://fig2026.org>

June 2026

ICCGIS 2026

14 - 19 June 2026
Nessebar, Bulgaria
<https://iccgis.cartography-gis.com>

New Earth-to-ocean navigation products by ComNav

ComNav Technology unveiled a new technological ecosystem for surveying under the theme "From Earth to Ocean". The ML300 mobile laser scanning system is designed for large-scale surveying projects and complex environments. It incorporates multi-mode fusion positioning technology, integrating GNSS, IMU, DMI and laser SLAM, providing a new approach to 3D scene reconstruction. The SV300 unmanned surface vessel was designed specifically for intelligent underwater surveying. The HYD10 is a lightweight, high-precision echo sounder designed for modern surveying tasks. www.comnavtech.com

First mass-produced car with Beidou system

Dongfeng Aeolus launched the first mass-produced passenger vehicle, the Sky EV01, equipped with China's Beidou satellite navigation system. It offers particularly strong signal coverage and precise positioning in the Asia-Pacific region.

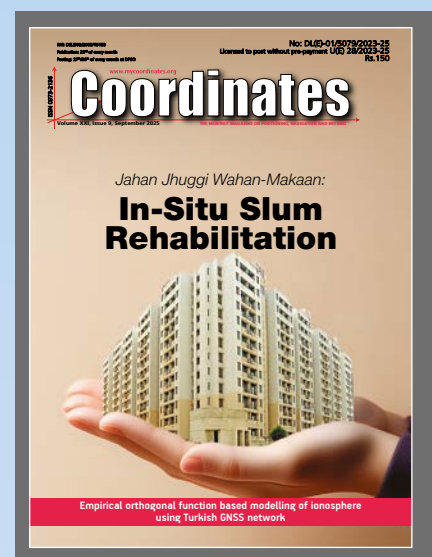
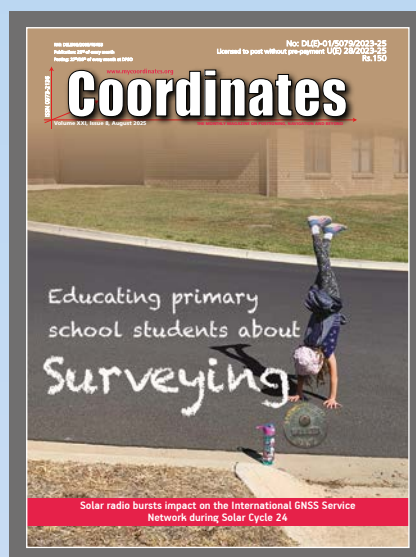
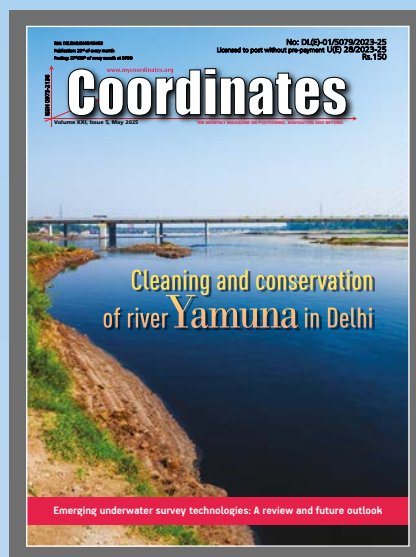
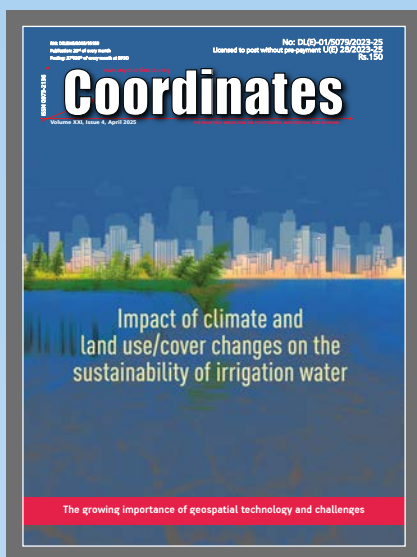
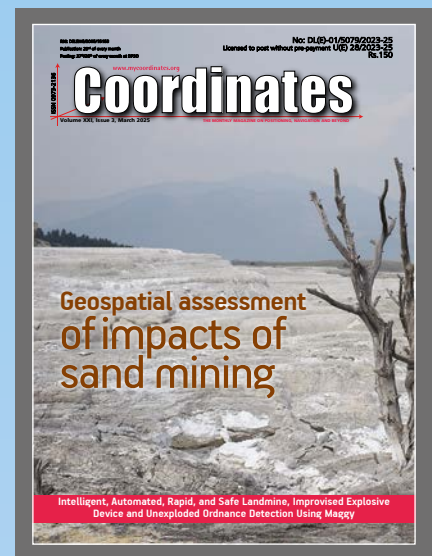
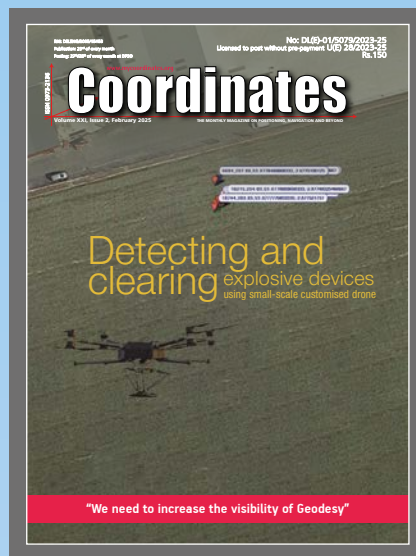
GNSS on-board units for European tolling

Norbit's Connectivity segment, Norway has received a new order for deliveries of GNSS on-board units to the European Electronic Toll Service (EETS) provider Toll4Europe.

Swift and RugGear partnership

Swift Navigation and RugGear have joined to embed high-accuracy positioning capabilities into RugGear's enterprise and mission-critical mobile devices.

The partnership integrates Swift Navigation's Skylark Precise Positioning Service directly into RugGear devices built on the Qualcomm Snapdragon 6 Gen Platform. This native integration delivers reliable lane-level accuracy — an order of magnitude improvement over standard GPS — without requiring any external receiver or configuration. ▽



“The monthly magazine on Positioning, Navigation and Beyond”
Download your copy of Coordinates at www.mycoordinates.org



Inertial Navigation Solutions

For Geospatial, Autonomous, & Defense applications:

- High-performance in the smallest package
- Reliable navigation and positioning everywhere
- Post-processing with Qinertia PPK software

*NavIC compatibility: Apogee, Ekinox, Navsight, Quanta series

